

A&A manuscript no.
(will be inserted by hand later)

Your thesaurus codes are:
03 (03.13.2; 11.09.1; 11.16.2; 11.19.4)

ASTRONOMY
AND
ASTROPHYSICS

Globular clusters in NGC 5128*

S. Holland¹, P. Côté^{2**}, and J. E. Hesser³

¹ Institut for Fysik og Astronomi (IFA), Aarhus Universitet, Ny Munkegade, Bygning 520, DK-8000 Århus C, Denmark, e-mail: holland@obs.aau.dk

² California Institute of Technology, Mail Stop 105-24, Pasadena, California, 91125 USA, e-mail: pc@astro.caltech.edu

³ Dominion Astrophysical Observatory, Herzberg Institute of Astrophysics, National Research Council, 5071 West Saanich Road, Victoria, B.C., V8X 4M6, Canada, e-mail: Jim.Hesser@hia.nrc.ca

Received 03 February 1999; accepted

Abstract. We used the Wide Field Planetary Camera 2 aboard the *Hubble Space Telescope* to search for globular clusters in the inner regions of the nearby giant elliptical galaxy NGC 5128. This galaxy is believed to be the product of a merger between a large elliptical galaxy and a small late-type spiral between 160 and 500 Myr ago. We identified 21 globular cluster candidates and measured their core radii, tidal radii, half-mass radii, ellipticities, position angles, and $V-I$ colors. We find evidence that the NGC 5128 globular cluster candidates are systematically more elliptical than are those of the Milky Way. Approximately half of the candidates have $(V-I)_0$ colors that are consistent with their being either old, unreddened globular clusters, similar to those found in the Milky Way, or young, reddened globular clusters that may have formed during the recent merger event. Most of the rest have colors that are consistent with their being old globular clusters similar to those found in the Milky Way. We find one blue object with $(V-I)_0 < 0.26 \pm 0.09$. The color, reddening, and integrated magnitude of this object are consistent with its being a small globular cluster with an age of ~ 100 Myr and a mass (based on its integrated luminosity) of $\leq 4000 M_\odot$. We find no evidence for bimodality in the colors of the globular cluster candidates in our sample beyond what can be explained by uncertainties in the differential reddening.

Key words: galaxies: individual (NGC 5128) – galaxies: peculiar – galaxies: star clusters – methods: data analysis

1. Introduction

Globular star clusters (GCs) are among the oldest stellar systems in the Universe and provide a powerful tracer of

Send offprint requests to: S. Holland

* Based in observations with the NASA/ESA *Hubble Space Telescope*, obtained at the Space Telescope Science Institute, which is operated by the Association of Universities for Research in Astronomy, Inc., under NASA contract NAS5-26555.

** Sherman M. Fairchild Fellow

the evolutionary history of a galaxy. There is strong evidence that massive star clusters can form during galactic mergers (e.g. Zepf & Ashman 1993; Schweizer et al. 1996), so galaxies that have recently experienced a merger event are ideal places to search for young GCs. Recently several candidates for luminous young GCs have been identified in various merging galaxies, such as NGC 3597 (Lutz 1991), NGC 1275 (Holtzman et al. 1992), and NGC 7252 (Schweizer & Seitzer 1993).

NGC 5128 (= Centaurus A, see Israel 1998 for a recent review) is classified as a giant S0pec galaxy. It is composed of a large, dominant spheroid, which itself resembles an E0 galaxy, and a disk that contains large amounts of gas and dust. Soria et al. (1996) used direct observations of resolved stars at the tip of the red giant branch in NGC 5128 to determine a true distance modulus of $\mu_0 = 27.8 \pm 0.2$, which corresponds to 3.6 ± 0.2 Mpc, making NGC 5128 the nearest giant elliptical galaxy to our own. There is strong evidence (see the review by Ebneter & Balick 1983) that it is the product of a recent merger between a large elliptical galaxy and a small late-type spiral. A thick dust band is seen across the center of NGC 5128 and there is evidence for significant star formation occurring in the central regions of the galaxy. G. Harris et al. (1999) used *Hubble Space Telescope* (*HST*) Wide Field Planetary Camera 2 (WFPC2) images to obtain a color–magnitude diagram for the outer halo of NGC 5128. They found a distance of 3.9 ± 0.3 Mpc, consistent with the Soria et al. (1996) estimate, and a population of old stars with iron abundances between $[\text{Fe}/\text{H}] \sim -2$ and $[\text{Fe}/\text{H}] \sim +0.2$. Their metallicity distribution function is consistent with two bursts of star formation. The first having $[\text{m}/\text{H}] = -0.6$ and producing approximately one-third of the stars, and the second having $[\text{m}/\text{H}] = 0$ and producing approximately two-thirds of the stars. They argue that the second burst of star formation occurred at least 1–2 Gyr after the first.

The first observation of a GC in NGC 5128 was by Graham & Philips (1980). The galaxy is now believed to have ~ 1700 GCs (H. Harris et al. 1984), with 87 confirmed spectroscopically (see H. Harris et al. 1988;

Sharples 1988). Recently G. Harris et al. (1998) used *HST* WFPC2 images to construct a color–magnitude diagram for C44, a GC in the halo of NGC 5128. They found that this GC was an old, intermediate-metallicity object similar to the GCs in the Milky Way. G. Harris et al. (1992, hereafter referred to as HG92) used Washington CMT_1T_2 photometry to derive metallicities for 62 of confirmed GCs in NGC 5128 and found a mean iron abundance of $[\text{Fe}/\text{H}] = -0.8 \pm 0.2$, which suggest that the NGC 5128 GC system is ~ 3 times more metal rich than the Milky Way GC system. They found no evidence for any GCs having metallicities significantly greater than those found in the Milky Way GCs. Such metal-rich GCs might be expected if some of the NGC 5128 GCs had formed recently in a gas-rich merger event. HG92 do, however, suggest that several blue GCs in NGC 5128 may be analogues of the intermediate-age GCs found in the Magellanic Clouds. On the other hand, Zepf & Ashman (1993) suggest that the metallicity distribution of the NGC 5128 GCs is bimodal, with the high-metallicity peak at $[\text{Fe}/\text{H}] = +0.25$ due to GCs formed in a merger. Hui et al. (1995) analyzed the kinematics of the NGC 5128 GC system and found that the metal-rich GCs are part of a dynamically separate system from the metal-poor GCs. Numerical simulations suggest that the merger event occurred between 160 (Quillen et al. 1993) and 500 ($D/5$ Mpc) Myr ago, where D is the distance to NGC 5128 in Mpc (Tubbs 1980). This suggests that any GCs that formed in *this particular* merger should be quite young and, therefore, rather blue ($\sim 0.4 < V-I < 0.6$; see Sect. 5).

Minniti et al. (1996) and Alonso & Minniti (1997, hereafter referred to as AM97) used *HST* Wide-Field/Planetary-Camera 1 (WF/PC-1) images, taken before the corrective optics package was installed in 1993, to search for GCs in the inner regions of NGC 5128. They identified 125 GC candidates, young associations, and open cluster candidates in the inner three kpc of NGC 5128. They also used ground-based *RK* photometry to estimate metallicities for 47 GC candidates. Schreier et al. (1996) found 74 compact sources along the northern edge of the NGC 5128 dust lane using *HST* WF/PC-1 images. They estimate that most of these sources are young stars (spectral class A or earlier) but note that some are resolved and may be GCs.

Identifying GC candidates in the inner regions of NGC 5128 is difficult since there is nonuniform extinction, contamination from foreground stars and background galaxies, and confusion with open clusters and blue, star-forming knots in NGC 5128. GC candidates can not be identified based solely on their colors since the large amount of uneven reddening makes it very difficult to determine the dereddened color of an object. A better approach is a scheme to identify GC candidates based solely on their structural parameters. All known GCs in the Local Group can be reasonably well fit by Michie–King models (Michie 1963; King 1966), although $\sim 20\%$

Table 1. Log of the observations.

Field	$\alpha(\text{J2000})$	$\delta(\text{J2000})$	Filter	Exposure
1	$13^{\text{h}}25^{\text{m}}33^{\text{s}}.5$	$-43^{\circ}00'14''$	F555W	3×60
			F814W	3×60
2	$13^{\text{h}}25^{\text{m}}28^{\text{s}}.1$	$-43^{\circ}00'14''$	F555W	4×60
			F814W	3×60
3	$13^{\text{h}}25^{\text{m}}22^{\text{s}}.7$	$-43^{\circ}00'14''$	F555W	3×60
			F814W	3×60
4	$13^{\text{h}}25^{\text{m}}33^{\text{s}}.6$	$-43^{\circ}02'14''$	F555W	3×40
			F814W	3×40
5	$13^{\text{h}}25^{\text{m}}28^{\text{s}}.2$	$-43^{\circ}02'14''$	F555W	3×60
			F814W	3×50
6	$13^{\text{h}}25^{\text{m}}22^{\text{s}}.7$	$-43^{\circ}02'14''$	F555W	3×60
			F814W	3×60

show evidence of having undergone core collapse. The vast majority of the Milky Way’s GCs are uniformly old objects with ages of 11.5 ± 1.3 Gyr (Chaboyer et al. 1998), mean King core radii of $r_c = 2.3 \pm 0.4$ pc, mean King tidal radii of $r_t = 45.2 \pm 3.5$ pc, mean concentrations of $c \equiv \log_{10}(r_t/r_c) = 1.40 \pm 0.04$, and mean ellipticities of $\epsilon = 0.08 \pm 0.01$. If the GCs in NGC 5128 are structurally similar to those in the Local Group spiral and dwarf galaxies, then high resolution imaging can be used to identify GC candidates in the inner regions of NGC 5128 without resorting to an identification scheme based upon the integrated colors of the objects.

2. The Data

2.1. Observations

We used the WFPC2 aboard the *HST* to obtain F555W (WFPC2 broadband V) and F814W (WFPC2 broadband I) images of a region near the nucleus of NGC 5128. The data were obtained on July 27, 1997 for the cycle 6 program GO-6789. The WFPC2 had an operating temperature of -88°C and a nominal gain setting of $7 \text{ e}^-/\text{ADU}$. The observations are listed in Table 1.

Exposures were taken in each field with each of the F555W and the F814W filters. Cosmic rays impact ~ 20 pixels per second on each WFPC2 CCD, but by combining the multiple exposures per filter for each field, the number of pixels lost to cosmic ray events is negligible. Therefore, we did not apply any processing explicitly to remove cosmic rays from the images. The data were preprocessed through the standard STScI pipeline for WFPC2 data. Known bad pixels were flagged and not used in the data analysis. No corrections were made for geometric distortions in the area of the WFPC2 pixels.

The survey consists of six fields that cover a total area of approximately 5.3×8.0 centered on $\alpha = 13^{\text{h}}25^{\text{m}}27^{\text{s}}.3$, $\delta = -43^{\circ}01'09''$ (J2000 coordinates), the nu-

cleus of NGC 5128. Adjacent fields overlap by ~ 0.5 giving a total effective area of $\sim 25 \square'$ for the survey.

2.2. Data Reductions

We combined the exposures for each field by taking the average of the three images in each filter (four images for the F555W exposures of Field 2). No re-registration of the images was performed since the shifts between the images were typically less than 0.1 pixel (0.01 on the WFC and 0.005 on the PC). We estimate that combining the images in this way may result in the sizes of the GC candidates being systematically overestimated by no more than ~ 0.02 . We prefer to introduce this simple systematic offset than deal with the poorly-understood systematic uncertainties that arise from interpolating flux across fractional-pixel shifts.

2.2.1. Identifying Globular Cluster Candidates

At the distance of NGC 5128 ($d = 3.6 \pm 0.2$ Mpc), the mean King core- and tidal-radii of the Milky Way GCs would appear to be $\bar{r}_c = 0.13 \pm 0.02$ and $\bar{r}_t = 2.59 \pm 0.20$, respectively. Therefore, any GCs in NGC 5128 will appear to be semi-stellar and be strongly affected by the point spread function (PSF) of the WFPC2. After some experimentation, we adopted the following procedure for identifying GC candidates. We wish to stress that this procedure is quite strict and will probably result in the rejection of some legitimate GC candidates. However, we prefer to reject real GCs rather than have our sample contaminated with stars or background galaxies.

In order to increase the signal-to-noise ratio (S/N) of the GC candidates – a particularly important point for the faint ($V < 20$) GC candidates – we combined the F555W and F814W images for each field to get finding images. The dust lane introduces variations in the background on spatial scales of $\sim 1''$, comparable to the expected sizes of the GC candidates in NGC 5128. To reduce the effects of the uneven background light, large-scale spatial variations in the background were removed by running a ring median filter (Secker 1995) over the finding image, subtracting the resulting smoothed background, and adding back the mean background value. The median filter radius was set to $1''$, which is ~ 3.5 times the expected full-width at half maximum (FWHM) of a typical GC candidate. This choice of filter radius ensures that the cores of the GC candidates will not be altered by the median filter and that any background structure larger than a typical GC candidate will be removed. Since the most extended Milky Way GCs have tidal radii that are significantly greater than 2.5 times their FWHM, and extended halos have been detected around several Galactic and extra-Galactic GCs (Grillmair et al. 1995; 1996; Holland et al. 1997), this approach will alter the distribution of light in the outer regions of most of the GC candidates. However, this

is not important since the finding images are used *only* to construct a preliminary list of GC candidates. A more rigorous set of criteria, based on the structures of the GC candidates as determined from the *original* images, will be applied to the preliminary list to obtain a final list of GC candidates in the central regions of NGC 5128.

The first step in our identification procedure was to run the DAOPHOT II (Stetson 1987; 1994) FIND routine on the background-subtracted images to identify GC candidates. The finding thresholds were set to $6\sigma_{\text{sky}}$ for the PC images and $10\sigma_{\text{sky}}$ for the WFC images. Tests with artificial GCs suggested that any detections below these thresholds would be rejected at some point in our identification process. DAOPHOT II FIND has an algorithm for rejecting non-stellar objects based on two parameters called “sharpness” and “round”. This algorithm was turned off since images of GCs can have different shapes and concentrations from images of stars.

Next, the DAOPHOT II PHOTOMETRY routine was used to obtain aperture photometry for each of these detections. The photometry was performed separately on each of the combined F555W and F814W frames, *not* on the combined finding frame. An aperture radius of 0.2 was used since most Galactic GCs, if moved to the distance of NGC 5128, would appear to have core radii smaller than this. Therefore, the signal within the aperture will be dominated by the light from the object and not from the background. Candidate objects with $S/N < 5$ within the photometry aperture were discarded since the signal was not strong enough to determine reliable shape parameters. The sky brightness was determined in an annulus with an inner radius of ~ 0.9 and an outer radius of ~ 1.1 . This annulus was chosen to be far enough from the center of the GC candidate that the light in the annulus will be dominated by the background, yet near enough to the GC candidate that the light in the annulus will be a reasonable approximation of the mean background at the location of the object. For large GC candidates this annulus will be inside the tidal radius of the object so our estimate of the background will be contaminated. However, the values determined at this stage are only preliminary estimates, which will be improved upon later in the identification process when Michie–King models are fit to the GC candidates. The lists of GC candidates in each of the F555W and F814W images were matched using the DAOMATCH and DAOMASTER software. Only objects that appeared in *both* the F555W and F814W images, and whose centers matched to within 0.05 (~ 1.1 pixel on the PC images and ~ 0.5 pix on the WFC images), were considered to be real GC candidates.

Distinguishing bona fide GCs from stars and background galaxies is challenging. The colors of the objects can not be used since we are interested in studying the color distribution of GCs in NGC 5128 and do not wish to bias our sample. To make matters worse, the presence of dust in NGC 5128 will add a significant amount of scatter

to the intrinsic color distribution, and may cause legitimate GCs to be rejected if a color-based identification scheme is used. The solution is to identify GC candidates by their structural parameters, although the best choice of structural parameters is not obvious. At the distance of NGC 5128 a typical Galactic GC would appear to have an intrinsic FWHM of $\sim 0''.25$, or approximately twice the FWHM of the WFPC2 PSFs. Therefore, the observed FWHM, concentration, and ellipticity of a GC candidate can be heavily influenced by the PSF. Since the PSF varies strongly with position on the WFPC2 CCDs, the potential for confusion between stellar images and concentrated GC candidates is great if the PSF is not removed, in some way, from the data. Therefore, the observed shape of an object can not be directly used to classify it as a star, GC candidate, or galaxy.

After some experimentation with adding and recovering artificial GCs and artificial stars, we found that the following procedure was reasonably reliable for identifying GC candidates. For each GC candidate we took all the pixel values within $1''$ of the center of the object and subtracted an estimate of the local background (the center and background were determined by the DAOPHOT II PHOTOMETRY algorithm). A one-dimensional Moffatian (Moffat 1969),

$$M(r_{\text{eff}}) = M(0) \left[1 + \left(\frac{r_{\text{eff}}}{\alpha} \right)^2 \right]^{-\beta}, \quad (1)$$

was fit to each candidate using the effective radius, r_{eff} , instead of the true distance from the center of the candidate in order to compensate for any ellipticity that might be introduced by the PSF. The effective radius of an ellipse is defined by $ab\pi \equiv r_{\text{eff}}^2\pi$, where a and b are the lengths of the semi-major and semi-minor axes of the ellipse, respectively. For each pixel the effective radius from the center of the GC candidate was computed using:

$$\begin{aligned} r_{\text{eff}}^2 = & x^2 \left[(1 - \epsilon)^2 \cos^2 \theta_0 + \sin^2 \theta_0 \right] / (1 - \epsilon) \\ & + y^2 \left[\cos^2 \theta_0 + (1 - \epsilon)^2 \sin^2 \theta_0 \right] / (1 - \epsilon) \\ & + 2xy\epsilon(\epsilon - 2) \cos \theta_0 \sin \theta_0 / (1 - \epsilon), \end{aligned} \quad (2)$$

where x and y are the coordinates of the pixel on the CCD, and ϵ and θ_0 are estimates of the ellipticity and position angle of the GC candidate. The latter two quantities were estimated from the moments of the light from each object.

In order to determine which combinations of α and β corresponded to stars and which corresponded to GC candidates, a series of artificial stars and artificial GCs were added to the images. The artificial stars were added using the DAOPHOT II ADDSTAR routine and the appropriate PSFs scaled to magnitudes of $16 \leq F555W \leq 22$. The artificial GCs, also with integrated magnitudes of $16 \leq$

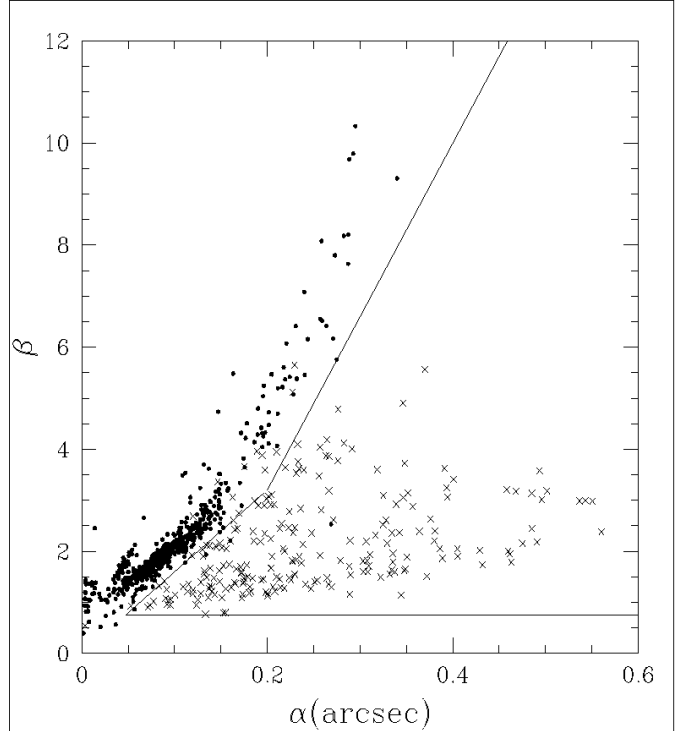


Fig. 1. This figure shows the best-fitting Moffatian α and β parameters for the artificial stars (circles) and artificial GCs (crosses). Based on the distribution of objects in this diagram we assumed that any objects that lie inside the wedge formed by the solid lines were GC candidates. No upper limit was placed on the value of β .

$F555W \leq 22$, were added using the IRAF¹ v2.10.4 task NOAO.ARTDATA.MKOBJECT. The artificial GCs all had ellipticities of $\epsilon = 0$, concentrations of $0.67 \leq c \leq 2.12$, and core radii of $0''.067 \leq r_c \leq 0''.4$ (corresponding to physical core radii of between ~ 1 and ~ 7 pc at the distance of NGC 5128). Therefore, the artificial GCs had a range of structures similar to those of the Milky Way's GCs. The procedure described above was used to determine the Moffat α and β for each artificial object. The results are presented in Fig. 1 and were used to determine which combinations of α and β represent stars and which represent GC candidates. These limits on α and β were then applied to the GC candidates found on the WFPC2 images of NGC 5128.

Figs. 2 and 3 show the Moffatian α and β parameters for the ~ 3800 objects that were successfully fit by Moffatians. There are 403 objects with Moffat parameters that lie inside the wedge (see Fig. 1). Our simulated data suggest that these are extended objects such as GCs, background galaxies, dust features, open clusters, star forming regions, or blended stars.

¹ Image Reduction and Analysis Facility (IRAF), a software system distributed by the National Optical Astronomy Observatories (NOAO).

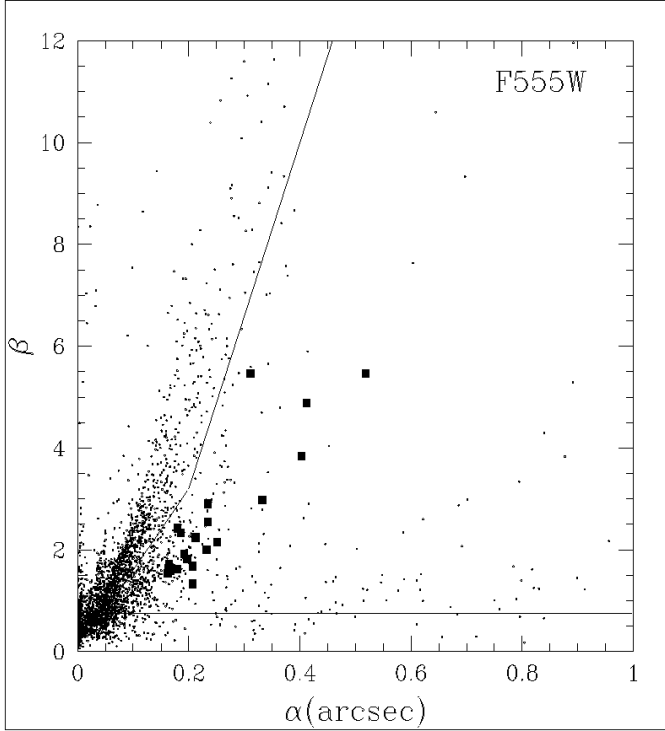


Fig. 2. This figure shows the best-fitting Moffatian α and β parameters for each object (small circles) on the F555W images. Simulated data (see Fig. 1) suggest that objects that lie inside the wedge formed by the solid lines are extended objects. Therefore we consider any objects that lie inside the wedge to to be GC candidates. The solid squares show the locations of the GC candidates from Table 2.

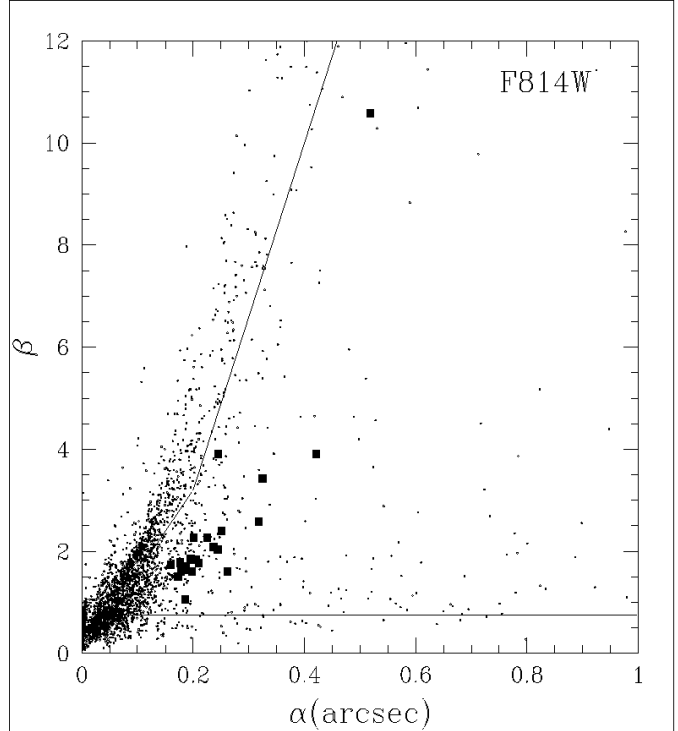


Fig. 3. This figure shows the best-fitting Moffatian α and β parameters for each object (small circles) on the F814W images. Simulated data (see Fig. 1) suggest that objects that lie inside the wedge formed by the solid lines are extended objects. Therefore we consider any objects that lie inside the wedge to to be GC candidates. The solid squares show the locations of the GC candidates from Table 2.

2.2.2. Fitting Michie–King Models

We fit a two-dimensional, PSF-convolved, single-mass Michie–King model to each of the 403 GC candidate using software developed by Holland (1997). This software assumes that the surface brightness profile along the effective radius axis of a GC candidate with an ellipticity of ϵ and a position angle of θ_0 has a King profile with a concentration of c and a core radius of r_c . It then builds a two-dimensional model based on this surface brightness profile, ϵ , and θ_0 . The two-dimensional model is convolved with the appropriate PSF for the location on the CCD and a chi-square minimization is performed between the PSF-convolved model and the original data image. The software uses CERN’s MINUIT function minimization package to fit simultaneously the concentration, core radius, total flux in the object, ellipticity, position angle, and mean background. Objects located within 32 pixels of the edge of a CCD ($= 3''.2$ for the WFC and $1''.6$ for the PC) were not fit to avoid the edges of the CCD biasing the fits. Once a best fit had been determined, the King tidal radius, r_t , and the half-mass radius, r_h , of the model were computed.

Separate fits were made to the F555W images and the F814W images and an object was considered to be GC

candidate only if a Michie–King model could be fit in both colors. We were able to fit Michie–King models to 98 of the 403 potential GC candidates. Mean structural parameters were calculated for these object by taking the mean of the values found in each filter. Four objects (#8, #113, #128, and #129) (see Tables 2, 3, and 4) were identified on multiple fields. In these cases we computed the mean of the structural parameters measured in each field.

We elected to separate GC candidates from background galaxies based on their fitted ellipticities and half-mass radii (see Fig. 4). Half-mass radii are preferred to tidal radii or core radii because Fokker–Planck models of spherical stellar systems show that half-mass radii remain reasonably constant over periods of several Gyr (e.g. Cohn 1979; Takahashi 1997), making it a unique length scale for GCs. The mass interior to the half-mass radius tends to undergo a gravo-thermal collapse and become concentrated at the center of the GC over time (i.e. core-collapse), which results in the core radius shrinking. Meanwhile, the mass exterior to the half-mass radius tends to expand outwards, causing the tidal radius to grow. Since we are interested in finding young, intermediate-age, and old GCs in NGC 5128, it is useful to have a selection criterion that does not depend on the age

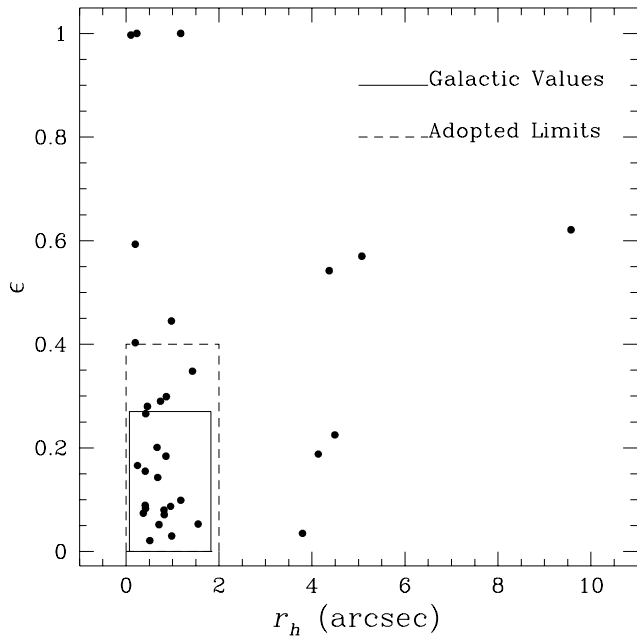


Fig. 4. The ellipticity vs. half-mass radius of the best-fitting single-mass Michie–King model for each object where a Michie–King model was successfully fit. Objects with $r_h > 10''$ (~ 175 pc) have not been plotted. The solid box in the lower left of the plot shows the region occupied by Galactic GCs. Based on this plot we have assumed that any object with $r_h < 2''$ (~ 35 pc) and $\epsilon < 0.4$ (the dashed box) is a GC candidate in the NGC 5128 system.

of the GC candidate. Galactic GCs have half-mass radii of approximately $1.3 < r_h < 31.9$ pc (W. Harris 1996), which corresponds to $0''.07 < r_h < 1''.83$ at the distance of NGC 5128. There is no evidence that the radius of a Galactic GC depends on its mass (van den Bergh et al. 1991). Therefore, we have assumed that only objects with $r_h \leq 2''$ (~ 35 pc at the distance of NGC 5128) were GC candidates. It is possible that some of the objects in Fig. 4 that have high ellipticities and low half-mass radii are double clusters. However, Innanen et al. 1983 have shown that a binary GC could not survive a single Galactic orbit in the Milky Way so it is unlikely that there are any old, or intermediate-age double GCs in NGC 5128. It is possible that very young multiple GCs that formed within the last $\sim 100 - 200$ Gyr could have survived to the present day, but we are unable to differentiate between them and background galaxies.

The most elliptical Galactic GC is M19 with $\epsilon = 0.27$ (White & Shawl 1987) and the most elliptical GC known is NGC 2193 in the Large Magellanic Cloud (LMC) which has $\epsilon = 0.33$ (Geisler & Hodge 1980). Geisler & Hodge (1980) modelled the distribution of observed ellipticities for 25 GCs in the LMC and found that it was unlikely that the largest true ellipticity exceeded $\epsilon = 0.4$. The LMC contains both dynamically young and dynam-

Fig. 5. A finding chart for Field 1. The GC candidates are circled with their identification numbers (see Table 2) printed near each object.

Fig. 6. A finding chart for Field 2.

Fig. 7. A finding chart for Field 3.

Fig. 8. A finding chart for Field 4.

cally old GCs, so the largest ellipticity seen in the LMC is a reasonable estimate of the largest ellipticity that we can expect to see in NGC 5128. Therefore, only objects with $\epsilon \leq 0.4$ were considered to be GC candidates.

The final step was to examine visually the WFPC2 images of each GC candidate to ensure that the Michie–King model fits looked realistic. We found that $\sim 20\%$ of the objects were either located on diffraction spikes from saturated stars, or exhibited unusually large residuals when the best-fitting Michie–King models were subtracted. These spurious identifications were discarded.

Fig. 4 shows the measured half-mass radii and ellipticities for the surviving objects in NGC 5128 and Table 2 shows the final list of GC candidates that we find in the central regions of NGC 5128. The second and third columns show the J2000 coordinates of the objects as determined using the IRAF/STSDAS (v2.0.1) task STSDAS.TOOLBOX.IMGTOOLS.XY2RD. Column 4 is the observed (projected) distance of the GC candidate from the center of NGC 5128 in arcminutes. The center of NGC 5128 was taken to be $\alpha_{J2000} = 13^{\text{h}}25^{\text{m}}27^{\text{s}}.3$, $\delta_{J2000} = -43^{\circ}01'09''$ (Johnston et al. 1995). Columns 5 and 6 give the field (from Table 1) and CCD that the object was found on. Columns 7 and 8 give the X and Y coordinates (in pixels) on the CCD. Column 9 lists the identification number of the object in Table 1 of Minniti et al. (1996).

Tables 3 and 4 lists the coordinates for the 61 extended objects with $r_h > 2'$ and $\epsilon > 0.4$. Some of these objects may be GCs in NGC 5128 while others may be background galaxies with structures similar to those of Michie–King models. Six of these objects have been previously identified as GCs by Minniti et al. (1996) and Sharples (1988).

Figs. 5 through 10 show the locations of the 21 GC candidates on the F814W-band WFPC2 images. Only objects that pass all of the criteria described above are marked on these figures. Objects (such as #15) were only marked on the fields that they were identified as GC candidates in. In most of the cases where a GC candidate is present in multiple fields, but only identified in one field, the GC candidate was located very near the edge of one of the CCDs. Spatial variations in the PSF are largest near the edges of the CCDs so the Michie–King model fits are less reliable near the edges of the CCDs.

Table 2. The GC candidates in the central regions of NGC 5128.

ID	α_{J2000}	δ_{J2000}	D	Field	CCD	X	Y	Other
1	13 ^h 25 ^m 16 ^s .1	-42°59'45"	2'.50	3	3	703.990	570.660	...
2	13 ^h 25 ^m 16 ^s .4	-43°02'10"	2'.26	6	3	726.813	361.345	...
3	13 ^h 25 ^m 18 ^s .1	-43°01'59"	1'.90	6	3	516.154	406.027	...
4	13 ^h 25 ^m 19 ^s .4	-43°01'13"	1'.47	3	2	482.000	599.000	...
5	13 ^h 25 ^m 20 ^s .5	-43°00'52"	1'.30	3	2	310.789	429.262	...
6	13 ^h 25 ^m 25 ^s .3	-43°02'01"	0'.95	5	3	341.557	317.009	...
7	13 ^h 25 ^m 26 ^s .6	-42°59'27"	1'.71	1	3	686.555	752.859	M27
8	13 ^h 25 ^m 27 ^s .0	-43°00'02"	1'.12	1	3	746.948	397.874	M26
8	13 ^h 25 ^m 27 ^s .0	-43°00'02"	1'.12	2	3	171.527	228.000	M26
9	13 ^h 25 ^m 27 ^s .1	-42°59'40"	1'.49	2	3	101.013	438.000	M25
10	13 ^h 25 ^m 27 ^s .2	-42°59'28"	1'.69	1	3	621.989	725.544	M24
11	13 ^h 25 ^m 27 ^s .2	-43°01'54"	0'.75	4	3	672.131	515.204	...
12	13 ^h 25 ^m 27 ^s .8	-42°59'23"	1'.77	1	3	551.791	755.891	M23
13	13 ^h 25 ^m 28 ^s .5	-43°02'57"	1'.81	5	2	432.822	211.852	...
14	13 ^h 25 ^m 29 ^s .2	-43°00'16"	0'.94	1	3	553.540	198.363	M20
15	13 ^h 25 ^m 29 ^s .8	-43°00'07"	1'.12	1	3	463.865	268.523	M18
16	13 ^h 25 ^m 30 ^s .2	-42°59'36"	1'.63	1	3	337.483	548.311	M17
17	13 ^h 25 ^m 31 ^s .1	-42°59'39"	1'.65	1	3	243.088	494.704	...
18	13 ^h 25 ^m 31 ^s .5	-43°00'04"	1'.32	1	3	280.111	236.550	M15
19	13 ^h 25 ^m 31 ^s .7	-43°00'35"	0'.97	1	2	160.847	343.070	...
20	13 ^h 25 ^m 33 ^s .7	-43°01'20"	1'.16	1	2	655.839	265.242	...
21	13 ^h 25 ^m 34 ^s .4	-43°03'30"	2'.67	4	2	763.000	276.549	...

Fig. 9. A finding chart for Field 5.**Fig. 10.** A finding chart for Field 6.

The structural parameters of the best-fitting Michie–King models, as well as the fitted ellipticities and position angles, for each GC candidate are listed in Table 5. The first column contains the object ID (from Table 2). The various radii are given in units of seconds of arc, and the position angles are measured in degrees with $\theta_0 = 0^\circ$ being north and θ_0 increasing to the east. The χ^2_ν values are the reduced goodness of fit values returned by the fitting software. The uncertainties (σ) are the standard deviations in the values for the parameters that were measured in each filter. The position angles for GC candidates with small ellipticities (< 0.05) are not reliable. All of the χ^2_ν are significantly less than one, which suggests that the formal uncertainties in the model’s parameters are not reliable. Therefore, we have elected to estimate the uncertainties in the fits through monte-carlo simulations as described in Sect. 2.4.

2.3. Contamination

Our data will contain images of Galactic foreground stars, and supergiants in NGC 5128. From the work of Bahcall & Soneira (1981) we expect to find ~ 700 Galactic stars with $I \leq 20$ in our fields. The brightest stars in the halo of NGC

5128 have $V \sim 24.5$ (Soria et al. 1996) while the brightest young stars in the central regions of NGC 5128 are expected to have approximately $18 < V < 21$. The morphological selection criteria that we applied to our data are very effective at rejecting stars (see Figs. 1, 2, and 3), and the *HST* images show all of the 21 GC candidates to be extended objects, so we believe that stellar contamination is not a problem in our data.

The galaxy counts of Tyson (1988) suggest that there will be ~ 10 background galaxies in our images down to $I \sim 20$. However, many of these galaxies will be obscured by the dust lane, so we will detect significantly fewer than this. The morphological criteria that we applied to obtain our list of GC candidates will reject any galaxies that are not morphologically similar to the GCs found in the Milky Way or LMC. AM97 used a comparison field located 30' northeast of the nucleus to estimate that $\sim 20\%$ of the objects that they detect in their search for GCs in the inner regions of NGC 5128 are foreground stars or background galaxies. Since the morphological criteria that we applied are stricter than those of AM97, we believe that 20% is a reasonable upper limit on the amount of contamination in our list of GC candidates.

2.4. Uncertainties in the Structural Parameters

The MINUIT package provides an estimate of the formal uncertainty in each parameter based on the covariance matrix of the fit. In general the formal uncertainties were

Table 3. Extended objects with $r_h > 2''$ and $\epsilon > 0.4$ in the central regions of NGC 5128

ID	α_{J2000}	δ_{J2000}	D	Field	CCD	X	Y	Other
101	13 ^h 25 ^m 19 ^s .3	-43°02'30"	2'00	6	3	508.484	64.127	G331
102	13 ^h 25 ^m 20 ^s .0	-43°01'56"	1'57	6	3	307.668	352.171	...
103	13 ^h 25 ^m 20 ^s .6	-43°01'11"	1'25	3	2	500.453	470.957	...
104	13 ^h 25 ^m 21 ^s .0	-42°59'25"	2'10	3	3	128.163	607.910	...
105	13 ^h 25 ^m 21 ^s .8	-43°01'26"	1'07	6	4	561.226	61.192	...
106	13 ^h 25 ^m 22 ^s .1	-43°00'39"	1'10	3	2	234.000	214.221	...
107	13 ^h 25 ^m 22 ^s .7	-43°00'39"	1'00	3	2	256.978	156.827	...
108	13 ^h 25 ^m 22 ^s .8	-43°00'40"	0'98	2	2	99.928	720.877	...
109	13 ^h 25 ^m 23 ^s .0	-43°01'18"	0'82	6	4	593.184	215.648	...
110	13 ^h 25 ^m 23 ^s .1	-43°00'50"	0'85	3	2	377.582	144.000	...
111	13 ^h 25 ^m 23 ^s .3	-43°01'48"	0'99	5	3	497.984	517.934	...
112	13 ^h 25 ^m 23 ^s .6	-43°01'34"	0'81	5	3	421.420	632.818	...
113	13 ^h 25 ^m 23 ^s .7	-43°00'47"	0'78	2	2	195.364	642.153	...
113	13 ^h 25 ^m 23 ^s .7	-43°00'47"	0'78	3	2	369.000	69.211	...
114	13 ^h 25 ^m 24 ^s .5	-43°01'05"	0'54	6	4	659.413	414.000	...
115	13 ^h 25 ^m 24 ^s .9	-43°00'20"	0'94	2	3	444.626	122.783	...
116	13 ^h 25 ^m 25 ^s .0	-42°59'40"	1'55	2	3	326.147	506.868	...
117	13 ^h 25 ^m 25 ^s .3	-43°02'01"	0'95	6	4	101.986	296.981	...
118	13 ^h 25 ^m 25 ^s .6	-43°00'58"	0'38	2	2	354.000	478.498	...
119	13 ^h 25 ^m 25 ^s .9	-43°00'57"	0'35	2	2	358.270	438.501	...
120	13 ^h 25 ^m 26 ^s .0	-43°02'16"	1'14	6	1	629.884	296.782	...
121	13 ^h 25 ^m 26 ^s .5	-42°59'55"	1'25	2	3	207.559	311.875	...
122	13 ^h 25 ^m 26 ^s .6	-42°59'27"	1'71	3	4	412.549	539.948	M27
123	13 ^h 25 ^m 26 ^s .6	-43°02'11"	1'04	5	3	241.413	170.644	...
124	13 ^h 25 ^m 26 ^s .8	-43°00'12"	0'97	2	3	224.417	144.083	...
125	13 ^h 25 ^m 26 ^s .9	-43°00'14"	0'93	2	3	214.154	115.666	...
126	13 ^h 25 ^m 27 ^s .1	-43°00'06"	1'06	1	3	744.088	355.292	...
127	13 ^h 25 ^m 27 ^s .1	-43°01'54"	0'75	5	3	125.479	305.598	...
128	13 ^h 25 ^m 27 ^s .3	-42°59'28"	1'69	2	3	45.380	554.534	M24
128	13 ^h 25 ^m 27 ^s .3	-42°59'28"	1'69	3	4	386.949	604.233	M24
129	13 ^h 25 ^m 27 ^s .3	-43°01'54"	0'75	5	3	113.000	300.561	...
129	13 ^h 25 ^m 27 ^s .3	-43°01'54"	0'75	6	4	87.553	525.160	...
130	13 ^h 25 ^m 27 ^s .4	-43°01'28"	0'31	2	2	711.369	371.000	...
131	13 ^h 25 ^m 27 ^s .7	-43°00'13"	0'93	1	3	698.887	273.893	...
132	13 ^h 25 ^m 27 ^s .8	-42°59'23"	1'77	2	4	582.795	98.323	...
133	13 ^h 25 ^m 28 ^s .3	-43°00'19"	0'85	1	3	658.173	199.939	...
134	13 ^h 25 ^m 28 ^s .3	-43°01'38"	0'51	5	4	408.000	133.199	...
135	13 ^h 25 ^m 28 ^s .5	-43°01'23"	0'30	5	4	536.658	206.354	...
136	13 ^h 25 ^m 29 ^s .0	-43°00'43"	0'52	2	2	323.925	78.964	...
137	13 ^h 25 ^m 29 ^s .2	-43°00'16"	0'94	2	1	162.995	99.487	...
138	13 ^h 25 ^m 29 ^s .2	-43°00'22"	0'85	1	3	570.063	142.000	...
139	13 ^h 25 ^m 29 ^s .2	-43°01'28"	0'45	4	3	374.195	675.000	...
140	13 ^h 25 ^m 29 ^s .2	-43°02'29"	1'37	4	3	599.716	108.340	...

$\sim 10\%$ of the best-fit value of each parameter. This is consistent with the uncertainties quoted in Table 5 that were determined from the differences between the best fitting structural parameters determined from the F555W images and the F814W images.

In order to test the formal uncertainty estimates, and to look for systematic differences between the recovered structural parameters and the true structural parameters of the NGC 5128 GC candidates, we constructed a series

of artificial GCs and added them to the NGC 5128 images. The total of 810 artificial GCs were added to the WFPC2 images with randomly assigned concentrations between $0.67 \leq c \leq 2.74$, core radii between $0''.07 \leq r_c \leq 0''.4$, ellipticities of $\epsilon = 0$, and magnitudes of $16 \leq F555W \leq 22$. We found that the recovered concentrations for the brightest artificial GCs ($16 \leq F555W \leq 18$) were within $\sim 5\%$ of their true values 95% of the time. For the faintest artificial GCs ($20 \leq F555W \leq 22$) the recovered values were

Table 4. Extended objects with $r_h > 2''$ and $\epsilon > 0.4$ in the central regions of NGC 5128, continued.

ID	α_{J2000}	δ_{J2000}	D	Field	CCD	X	Y	Other
141	13 ^h 25 ^m 29 ^s .2	−43°00′38″	0′.61	1	2	109.346	606.980	...
142	13 ^h 25 ^m 29 ^s .7	−43°01′14″	0′.42	1	2	470.698	664.338	...
143	13 ^h 25 ^m 29 ^s .8	−43°00′07″	1′.12	2	4	95.982	190.565	M18
144	13 ^h 25 ^m 30 ^s .0	−43°02′12″	1′.15	4	3	460.000	234.000	...
145	13 ^h 25 ^m 30 ^s .1	−43°02′09″	1′.11	4	3	430.157	264.000	...
146	13 ^h 25 ^m 30 ^s .3	−43°01′12″	0′.53	1	2	466.932	598.975	...
147	13 ^h 25 ^m 30 ^s .6	−43°00′24″	0′.95	1	3	432.260	75.170	...
148	13 ^h 25 ^m 31 ^s .1	−43°01′19″	0′.69	5	4	476.273	487.763	...
149	13 ^h 25 ^m 31 ^s .2	−43°01′19″	0′.71	1	2	567.825	517.798	...
150	13 ^h 25 ^m 31 ^s .3	−43°00′37″	0′.89	1	2	169.525	384.000	...
151	13 ^h 25 ^m 31 ^s .5	−43°00′05″	1′.30	2	4	66.422	375.512	M15
152	13 ^h 25 ^m 31 ^s .8	−43°01′56″	1′.12	5	4	100.413	429.480	...
153	13 ^h 25 ^m 32 ^s .6	−43°01′27″	0′.99	5	4	345.530	611.654	...
154	13 ^h 25 ^m 33 ^s .0	−42°59′05″	2′.31	1	4	761.480	131.378	M12
155	13 ^h 25 ^m 33 ^s .1	−42°59′05″	2′.32	2	4	595.554	709.645	...
156	13 ^h 25 ^m 33 ^s .2	−43°01′37″	1′.15	5	4	224.435	632.127	...
157	13 ^h 25 ^m 33 ^s .6	−43°01′20″	1′.14	5	4	373.122	735.354	...
158	13 ^h 25 ^m 34 ^s .6	−43°02′37″	1′.96	4	2	280.000	74.000	...
159	13 ^h 25 ^m 35 ^s .9	−42°59′50″	2′.04	1	4	233.755	300.782	...
150	13 ^h 25 ^m 37 ^s .0	−43°01′29″	1′.78	4	4	360.651	495.008	...
161	13 ^h 25 ^m 37 ^s .8	−43°01′18″	1′.90	4	4	433.330	620.504	...

within 22% of the true values 95% of the time. Systematic shifts were negligible for artificial GCs with concentrations greater than $c \sim 0.9$, but grew rapidly for artificial GCs with concentrations less than this. The uncertainties in the structural parameters increased as the concentration decreased. Other structural parameters behaved in very similar manners.

A second source of uncertainty in the fitted structural parameters is the uncertainty in the PSF. Each GC candidate was fitted with a Michie–King model that was convolved by an estimate of the PSF at the location of the object on the CCD. We used PSFs that were created by Peter Stetson (1996, private communication) from WFPC2 observations of stars in the Galactic GC ω Centauri. However, the NGC 5128 images were taken approximately three years after the ω Cen ones, so long-term variations in the focus of the WFPC2 (e.g. Suchkov & Casertano 1997) raise the possibility of a mismatch between the actual and adopted PSFs. If this is the case then the derived structural parameters would be in error, as the fitted Michie–King models were convolved with a PSF constructed using a slightly different focus from that of our images. In order to estimate the possible errors introduced by uncertainties in the PSF, we repeated the Michie–King model fitting procedure with the *wrong* PSFs. In other words, we fit Michie–King models to the GC candidates on the WF3 CCD using both the F555W and the F814W PSFs from the WF2, WF3, and WF4 CCDs. This gave us six estimates of the structural parameters of each object obtained using six variations of the WF PSF. For each of

these estimates we computed the difference between W_0 as determined using the correct PSF, and the five W_0 s determined using the incorrect PSFs (ΔW_0). We then computed the mean ($\overline{\Delta W_0}$) and standard error in the mean of these five values for each GC candidate. This gave us an estimate of the systematic uncertainty in the value of W_0 that we derived for each GC candidate. Finally, we computed the mean, standard error in the mean, and median of the individual $\overline{\Delta W_0}$ values for all the GC candidate. This gave an estimate of the systematic uncertainty for a typical GC candidate in our data. These values, along with analogous estimates of the systematic errors in the other structural parameters, are presented in Table 6. This technique is not mathematically rigorous since the variations in the PSF from one CCD to another, and from one filter to another, are not the same as the variations due to changes in the focus of the *HST* over a period of two or three years. However, Suchkov & Casertano (1997) find that long-term changes in focus introduce changes of a few percent in the photometric calibrations, which corresponds to changes of a few percent in the shape of the PSF. The variations in the PSF from one CCD to the next can be much larger than this so we believe that the systematic errors derived here represent an over-estimate of the true systematic errors introduced by possible long-term variations in the PSF.

3. Structural Parameters

Table 5. The best-fitting structural parameters for the NGC 5128 GC candidates. The values are the means of the structural parameters derived from the F555W and F814W images.

ID	$W_0 \pm \sigma$	$r_c \pm \sigma$	$r_h \pm \sigma$	$r_t \pm \sigma$	$c \pm \sigma$	$\epsilon \pm \sigma$	$\theta_0 \pm \sigma$	χ^2_ν
1	$6.2 \pm \dots$	$0''.067 \pm 0''.001$	$0''.681 \pm 0''.023$	$1''.317 \pm 0''.045$	1.3 ± 0.0	0.143 ± 0.015	$-7^\circ.9 \pm 2^\circ.8$	0.134
2	6.8 ± 0.3	$0''.053 \pm 0''.006$	$0''.816 \pm 0''.080$	$1''.582 \pm 0''.157$	1.5 ± 0.1	0.080 ± 0.008	$+64^\circ.2 \pm 3^\circ.9$	0.171
3	4.1 ± 1.1	$0''.113 \pm 0''.035$	$0''.423 \pm 0''.057$	$0''.801 \pm 0''.117$	0.9 ± 0.2	0.266 ± 0.058	$+72^\circ.4 \pm 19^\circ.7$	0.116
4	8.6 ± 0.2	$0''.024 \pm 0''.017$	$1''.177 \pm 0''.726$	$2''.286 \pm 1''.411$	2.0 ± 0.1	0.099 ± 0.136	$+4^\circ.3 \pm 16^\circ.4$	0.323
5	6.2 ± 4.1	$0''.070 \pm 0''.076$	$0''.741 \pm 0''.564$	$1''.425 \pm 1''.107$	1.4 ± 1.0	0.290 ± 0.132	$+71^\circ.7 \pm 2^\circ.5$	0.171
6	6.2 ± 0.2	$0''.140 \pm 0''.001$	$1''.428 \pm 0''.167$	$2''.761 \pm 0''.326$	1.3 ± 0.1	0.348 ± 0.123	$-28^\circ.9 \pm 0^\circ.7$	0.142
7	3.5 ± 1.2	$0''.149 \pm 0''.101$	$0''.413 \pm 0''.122$	$0''.777 \pm 0''.219$	0.8 ± 0.2	0.155 ± 0.023	$-44^\circ.9 \pm 13^\circ.0$	0.086
8	9.0 ± 0.2	$0''.014 \pm 0''.006$	$0''.452 \pm 0''.078$	$0''.871 \pm 0''.163$	2.0 ± 0.1	0.140 ± 0.084	$-30^\circ.7 \pm 32^\circ.9$	0.331
9	7.3 ± 0.1	$0''.033 \pm 0''.001$	$0''.708 \pm 0''.037$	$1''.375 \pm 0''.071$	1.6 ± 0.0	0.052 ± 0.059	$-79^\circ.3 \pm 78^\circ.5$	0.097
10	5.5 ± 0.6	$0''.091 \pm 0''.015$	$0''.667 \pm 0''.100$	$1''.283 \pm 0''.201$	1.1 ± 0.1	0.201 ± 0.004	$-54^\circ.3 \pm 6^\circ.2$	0.117
11	6.6 ± 1.0	$0''.102 \pm 0''.001$	$1''.551 \pm 0''.920$	$3''.008 \pm 1''.797$	1.4 ± 0.3	0.053 ± 0.004	$+21^\circ.5 \pm 16^\circ.0$	0.207
12	4.2 ± 1.0	$0''.092 \pm 0''.023$	$0''.371 \pm 0''.062$	$0''.704 \pm 0''.126$	0.9 ± 0.2	0.074 ± 0.002	$+80^\circ.2 \pm \dots$	0.082
13	7.3 ± 0.1	$0''.039 \pm 0''.001$	$0''.822 \pm 0''.029$	$1''.597 \pm 0''.057$	1.6 ± 0.0	0.071 ± 0.023	$-47^\circ.9 \pm 78^\circ.8$	0.066
14	8.0 ± 0.8	$0''.015 \pm 0''.009$	$0''.460 \pm 0''.045$	$0''.892 \pm 0''.087$	1.8 ± 0.2	0.280 ± 0.187	$+74^\circ.3 \pm 11^\circ.5$	0.361
15	4.8 ± 0.1	$0''.084 \pm 0''.006$	$0''.419 \pm 0''.014$	$0''.799 \pm 0''.026$	1.0 ± 0.0	0.083 ± 0.000	$-13^\circ.3 \pm 2^\circ.7$	0.120
16	7.2 ± 0.4	$0''.044 \pm 0''.009$	$0''.867 \pm 0''.041$	$1''.684 \pm 0''.081$	1.6 ± 0.1	0.299 ± 0.033	$-54^\circ.1 \pm 2^\circ.9$	0.080
17	4.7 ± 1.6	$0''.048 \pm 0''.018$	$0''.245 \pm 0''.076$	$0''.468 \pm 0''.154$	1.0 ± 0.3	0.166 ± 0.094	$-32^\circ.5 \pm \dots$	0.079
18	6.9 ± 0.0	$0''.062 \pm 0''.000$	$0''.982 \pm 0''.018$	$1''.904 \pm 0''.034$	1.5 ± 0.0	0.030 ± 0.016	$-50^\circ.2 \pm 15^\circ.6$	0.107
19	$5.0 \pm \dots$	$0''.123 \pm 0''.010$	$0''.711 \pm \dots$	$1''.360 \pm \dots$	$1.0 \pm \dots$	0.292 ± 0.015	$-10^\circ.6 \pm 19^\circ.7$	0.250
20	7.2 ± 1.0	$0''.050 \pm 0''.025$	$0''.958 \pm 0''.132$	$1''.860 \pm 0''.260$	1.6 ± 0.3	0.087 ± 0.063	$-26^\circ.2 \pm 7^\circ.1$	0.146
21	3.9 ± 2.0	$0''.138 \pm 0''.058$	$0''.511 \pm 0''.191$	$0''.970 \pm 0''.382$	0.8 ± 0.4	0.021 ± 0.029	$-51^\circ.4 \pm 43^\circ.6$	0.085

Table 6. Systematic errors due to uncertainties in the PSF.

Quantity	mean	se	median
ΔW_0	0.4	0.1	0.2
Δr_c	$0''.010$	$0''.003$	$0''.004$
Δr_h	$0''.079$	$0''.026$	$0''.030$
Δr_t	$0''.154$	$0''.051$	$0''.060$
Δc	0.1	0.0	0.0
$\Delta \epsilon$	0.024	0.004	0.022
$\Delta \theta_0$	$31^\circ.8$	$15^\circ.2$	$7^\circ.4$

3.1. Core Radii

Fig. 11 shows the distribution of King core radii for the NGC 5128 GC candidates and for the Milky Way GCs. The Milky Way GCs have been shifted to the distance of NGC 5128 and their core radii have been converted to arcseconds ($1'' = 17.45 \pm 0.97$ pc for $d = 3.6 \pm 0.2$ Mpc). Galactic GCs with a central brightness cusp (which is believed to be a signature of a collapsed core) have been omitted from the sample. The faintest GC candidate in our sample has an absolute total magnitude of $M_{V,\text{tot}} = -6.4 \pm 0.2$. In order to ensure that we are comparing similar objects we have excluded all Milky Way GCs fainter than $M_{V,\text{tot}} = -6.4$.

In order to facilitate a comparison between the two GC systems we plotted the fraction, $f_i = n_i/n$, of the

total number of GCs in each bin, n_i , where n is the total number of GCs in each data set. The uncertainty in f_i was computed from the Poisson uncertainties in the number of GCs in each bin, and in the total number of GCs using

$$\sigma_{f,i} = \frac{1}{n} \sqrt{n_i + \frac{n_i^2}{n}}. \quad (3)$$

The mean core radius for the 21 NGC 5128 GC candidates is $\bar{r}_c = 0''.07 \pm 0''.01$ (standard error) while the mean for the 73 selected Milky Way GCs is $\bar{r}_c = 0''.11 \pm 0''.01$ (se). A Kolmogorov–Smirnov (KS) test shows that we can reject the hypothesis that the two samples are drawn from the same distribution at the 46% confidence level. Therefore, there is no evidence that the core radii of the GC candidates in NGC 5128 are distributed differently from the core radii of the Milky Way GCs.

The most noticeable difference between the core radii of the NGC 5128 GC candidates and the core radii of the Milky Way GCs in Fig. 11 is the lack of a tail extending to large core radii in the NGC 5128 data. This may be an artifact of the small number (21) of NGC 5128 GC candidates in our sample. The mean of a distribution is sensitive to the presence of tails and outliers, but the median is much more robust against outliers. Therefore we computed the median core radius for each data set. Both the NGC 5128 GC candidates and the Milky Way GCs have median core radii of $[r_c] = 0''.07$ ($= 1.22$ pc, or ~ 0.7 pixels on the WF CCDs and 1.4 pixels on the PC CCD). The similarity in the median core radii suggests that the

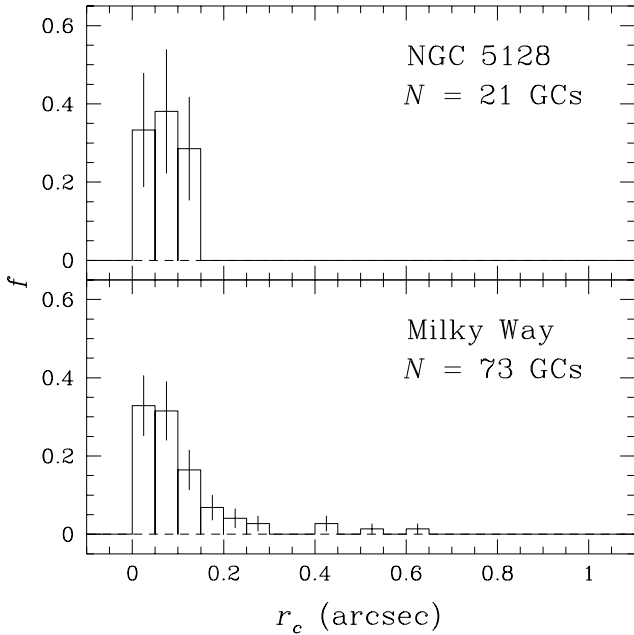


Fig. 11. This figure compares the distribution of core radii for GC candidates in NGC 5128 with the distribution of core radii for selected GCs (see Sect. 3.1) in the Milky Way. The vertical axis is the fraction of the total number of GCs and the error bars show the Poisson uncertainties in each bin.

“typical” core radius of a GC candidate in NGC 5128 is similar to that of the Milky Way GCs.

There may be systematic biases in the core radii that we have derived for the GC candidates in NGC 5128. Fitting Michie–King models to objects with core radii that are similar to the pixel scales of the images requires that the centers of the objects be accurately known. Small errors in determining the center of a candidate GC, and small systematic errors introduced by integrating Michie–King model profiles over the area of a pixel, may be sufficient to bias the fitted core radii towards smaller values. In addition to pixelation effects, the similarity between the core radii and the FWHMs of the PSFs may also be biasing our fits toward smaller core radii.

3.2. Tidal Radii

The tidal radius of a GC is affected by the gravitational potential of its parent galaxy (e.g., Innanen et al. 1983; Heggie & Ramamani 1995). In order to compare the tidal radii of GC candidates in NGC 5128 with those of GCs in the Milky Way it is necessary to correct for the tidal fields of both galaxies. The first step is to normalize the tidal radius of each GC candidate by its mass, \mathcal{M}_{cl} , to get $r_t/\mathcal{M}_{\text{cl}}^{1/3}$. If we assume that the gravitational potentials of

the Milky Way and NGC 5128 can be approximated by a spherical logarithmic potential of the form

$$\Phi = V_{\text{rot}}^2 \ln(R^2 + R_s^2) + \ln(C), \quad (4)$$

where R is the galactocentric distance, R_s is a scale length, and C is a constant, then we can compare the mean value of the normalized tidal radii of the GC candidates using

$$\frac{r_t}{\mathcal{M}_{\text{cl}}^{1/3}} = \left(\frac{R_p}{V_{\text{rot}}} \right)^{2/3} \left(\frac{G}{2g(e)} \right)^{1/3}, \quad (5)$$

where V_{rot} is the amplitude of the flat part of the rotation curve of the galaxy, G is the Newtonian gravitational constant, and $g(e)$ is a slowly varying function of the orbital eccentricity of the GC that has values of $g(0) = 1$ for circular orbits. The mean value of the normalized tidal radius of the GC candidates in NGC 5128, $\langle r_t/\mathcal{M}_{\text{cl}}^{1/3} \rangle$, can then be related to the mean normalized tidal radius of the Milky Way GCs by

$$\left\langle \frac{r_t}{\mathcal{M}_{\text{cl}}^{1/3}} \right\rangle = \left(\frac{V_{\text{rot,MW}}}{V_{\text{rot}}} \right)^{2/3} \left(\frac{g_{\text{MW}}(e)}{g(e)} \right)^{1/3} \frac{\langle R_p^{2/3} \rangle}{\langle R_{p,\text{MW}}^{2/3} \rangle} \left\langle \frac{r_t}{\mathcal{M}_{\text{cl}}^{1/3}} \right\rangle_{\text{MW}}, \quad (6)$$

where the subscript MW denotes the value for the Milky Way.

Eq. 6 assumes that the shape of the galactic potential is the same in both galaxies, but allows the total mass, as parameterized by V_{rot} , of each galaxy to vary. It also requires a knowledge of the distribution of GC orbits in each galaxy, as parameterized by $g(e)$ and R_p . We assumed a rotation velocity of $V_{\text{rot,MW}} = 220 \text{ km s}^{-1}$ for the Milky Way and $V_{\text{rot}} = 245 \text{ km s}^{-1}$ for NGC 5128 (Hui et al. 1995). The only information available on the distribution of orbits for GC candidates in NGC 5128 is the projected radial distances of the GC candidates from the center of NGC 5128, so we have assumed that the NGC 5128 GC system is dynamically similar to the Milky Way GC system. This involves two assumptions about the nature of the GC orbits. First, we assume that the mean eccentricity of the NGC 5128 GC orbits is the same as that for the Milky Way GCs ($\overline{e}_{\text{MW}} = 0.6 \pm 0.1$, Odenkirchen et al. 1997). Second, we assume that each GC is near the apogalacticon of its orbit, R_a , so $R \sim R_a$. This is a reasonable assumption since a GC having $e \sim 0.6$ spends $\sim 80\%$ of its time in the outer half of its orbit. An additional complication is that the observed galactocentric distance for a NGC 5128 GC candidate is the projection of the true galactocentric distance onto the plane of the sky. If we assume that the orbits are oriented randomly then R_a for a particular object’s orbit is most likely to be observed to lie at a projected distance of $D = (8/\pi^2)R_a$. Therefore, we estimated the perigalactic distances for each of the NGC

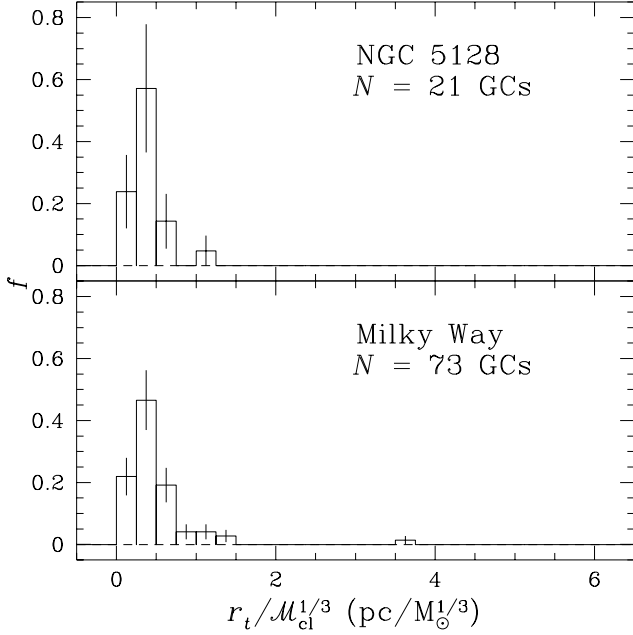


Fig. 12. This figure compares the distribution of normalized tidal radii (see Sect. 3.2) for GC candidates in NGC 5128 with the distribution of normalized tidal radii (after correcting for the difference in mass between the two galaxies) for GCs in the Milky Way. The vertical axis is the fraction of the total number of GCs and the error bars show the Poisson uncertainties in each bin.

5128 GC candidates from the observed distance from the center of NGC 5128 using

$$R_p = \frac{1 - e \pi^2}{1 + e \pi^2} D. \quad (7)$$

Fig. 12 shows the distribution of the normalized tidal radii for the NGC 5128 GC candidates and the Milky Way GCs. The cluster masses were computed from their total V -band luminosities assuming a mass-to-light ratio of two.

Our sample of GC candidates has $\langle r_t / \mathcal{M}_{cl}^{1/3} \rangle = 0.36 \pm 0.05$ (se) pc/M $_{\odot}^{1/3}$ ($N = 21$). The mean normalized tidal radius for 73 selected Milky Way GCs is $\langle r_t / \mathcal{M}_{cl}^{1/3} \rangle_{MW} = 0.69 \pm 0.08$ (se) pc/M $_{\odot}^{1/3}$. The multiplicative factor in Eq. 6 is 0.703, which yields a corrected $\langle r_t / \mathcal{M}_{cl}^{1/3} \rangle_{MW}$ of 0.49 ± 0.06 (se) pc/M $_{\odot}^{1/3}$. A KS test says that we can reject the hypothesis that the two samples are drawn from the same distribution at the 74% confidence level. Therefore, there is insufficient evidence to state that the distribution of the tidal radii of the NGC 5128 GC candidates differs from that of the Galactic GCs *if the difference in the masses of the two galaxies is taken into account*. However, we wish to stress that this calculation assumes that the distribution of GC orbits are statistically similar for both galaxies.

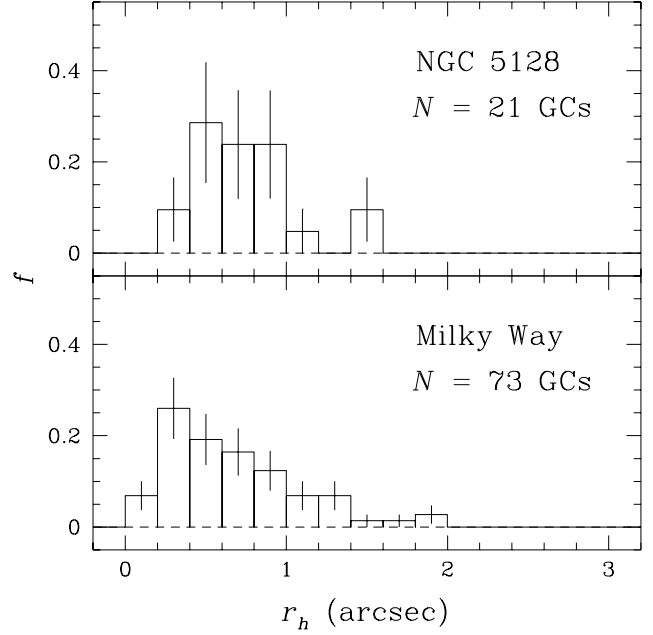


Fig. 13. This figure compares the distribution of half-mass radii for GC candidates in NGC 5128 with the distribution of half-mass radii for a subset of GCs in the Milky Way. The vertical axis is the fraction of the total number of GCs and the error bars show the Poisson uncertainties in each bin.

3.3. Half-Mass Radii

The distribution of half-mass radii for the NGC 5128 GC candidates is shown in Fig. 13 along with the same distribution for our subsample of 73 Milky Way GCs. The half-mass radii for the Milky Way GCs were determined by computing a Michie–King model (with concentrations and core radii taken from W. Harris 1996) for each Milky Way GC. This allowed us to make a direct comparison between the half-mass radii of the best-fitting single-mass Michie–King models for the NGC 5128 GC candidates and the half-mass radii of the best-fitting single-mass Michie–King models for the Milky Way GCs.

The mean half-mass radius for the 21 NGC 5128 GC candidates is $\bar{r}_h = 0''.73 \pm 0''.08$ (se) while the mean for 73 selected Milky Way GCs is $\bar{r}_h = 0''.67 \pm 0''.05$ (se). However, a KS test says that we can reject the hypothesis that the two samples are drawn from the same distribution at only the 74% confidence level, so there is no evidence that the distribution of half-mass radii in our sample of NGC 5128 GC candidates is different from that of the GCs in the Milky Way.

3.4. Ellipticities

The distribution of ellipticities for the NGC 5128 GC candidates is shown in Fig. 14. The 21 NGC 5128 objects have

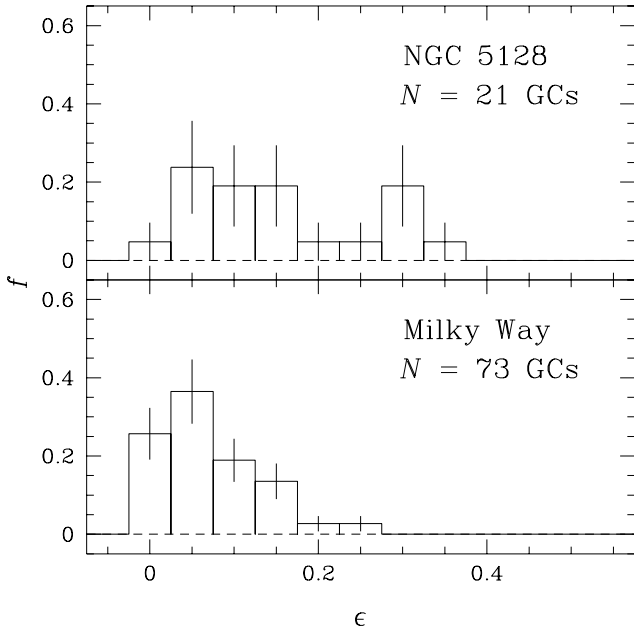


Fig. 14. The upper panel shows the distribution of ellipticities for the GC candidates in NGC 5128. The lower panel shows the distribution of ellipticities for the Milky Way’s GCs (from White & Shawl 1987).

$\bar{\epsilon} = 0.15 \pm 0.02$ (se) while the White & Shawl (1987) sample of Milky Way GCs yields $\bar{\epsilon} = 0.07 \pm 0.01$ (se) for the 73 Milky Way GCs. A KS test says that we can reject the hypothesis that the two samples are drawn from the same distribution at the 99.7% confidence level. Therefore, we conclude that the NGC 5128 GC candidates may have a different distribution of ellipticities from the Milky Way GCs.

The NGC 5128 GC candidates appear to be systematically more elliptical than the Milky Way GCs. There appears to be a lack of objects with low ellipticities and an excess of GC candidates with $\epsilon \sim 0.3$. The lack of GC candidates with $\epsilon \leq 0.05$ is probably due to the elliptical PSF not being fully removed from the data. Another possible source of ellipticity is the stochastic distribution of bright stars near the center of the object. Geisler & Hodge (1980) found that the random placement of stars with respect to the adopted center of a GC can introduce a systematic error in the observed ellipticity of $+0.045 \pm 0.015$ for GCs which are intrinsically spherical. This effect acts to make nearly spherical GCs appear to be more elliptical than they actually are. They also found that this systematic error decreases as the intrinsic ellipticity of the GCs increases. This would explain the lack of nearly circular GC candidates in NGC 5128, relative to the Milky Way.

AM97 identified 125 GC candidates in the inner $2/8 \times 2/8$ of NGC 5128. Table 7 lists the ellipticities from those GC candidates in common between the two studies. The

Table 7. A comparison of our ellipticities with those of AM97.

ID	AM97	Our $\epsilon \pm \sigma$	AM97 ϵ
9	M25	0.052 ± 0.059	0.02
10	M24	0.201 ± 0.004	0.09
12	M23	0.074 ± 0.002	0.04
14	M20	0.280 ± 0.187	0.06
15	M18	0.083 ± 0.000	0.05
16	M17	0.299 ± 0.033	0.14
18	M15	0.030 ± 0.016	0.09

mean difference between our ellipticities and the AM97 values is $\Delta\epsilon = \epsilon(\text{this work}) - \epsilon(\text{AM97}) = -0.024 \pm 0.041$.

3.5. Correlations of Cluster Properties with Distance

GCs live within the tidal field of their parent galaxy, and the properties of a GC may depend on its position within the protogalactic cloud at the time the GC formed (e.g. Murray & Lin 1992). In Fig. 15 we plot $\log_{10}(r_c)$, $\log_{10}(r_h)$ (both radii in arcseconds), c , and ϵ as functions of $\log_{10}(D)$, where D is the observed distance from the center of NGC 5128 in arcminutes. None of the properties show strong correlations with the distance from the center of NGC 5128, but the trends are qualitatively similar to the trends found by Djorgovski & Meylan (1994) for the same properties of the Milky Way’s GCs (see their Fig. 8). The correlations for $\log_{10}(r_c)$ and c for the NGC 5128 GC candidates are in the same sense as those for the Milky Way GCs, although Spearman rank correlation coefficients suggest that the correlations are weaker for the NGC 5128 GC candidates. This is to be expected because we are using the observed distance from the center of NGC 5128 (i.e. the distance projected onto the plane of the sky), while Djorgovski & Meylan (1994) used the true Galactocentric distance.

We find a weak trend for the half-mass radius of a GC candidate to decrease as the distance from the center of NGC 5128 increases, while the opposite trend is seen in the Milky Way. The Spearman rank correlation coefficient for our data is -0.356 , which corresponds to a significance of 0.887, while for the Milky Way GCs the correlation coefficient is $+0.478$. Therefore, there is insufficient evidence to for us to conclude that the observed trend for r_h to decrease as the galactocentric distance increases is real.

Djorgovski & Meylan (1994) found no correlation between the ellipticity of a GC and its Galactocentric distance. We find a correlation coefficient of -0.257 , corresponding to a significance of 0.739. An examination of Fig. 15, however, suggests that there is no significant correlation between ellipticity and galactocentric distance for the NGC 5128 GC candidates.

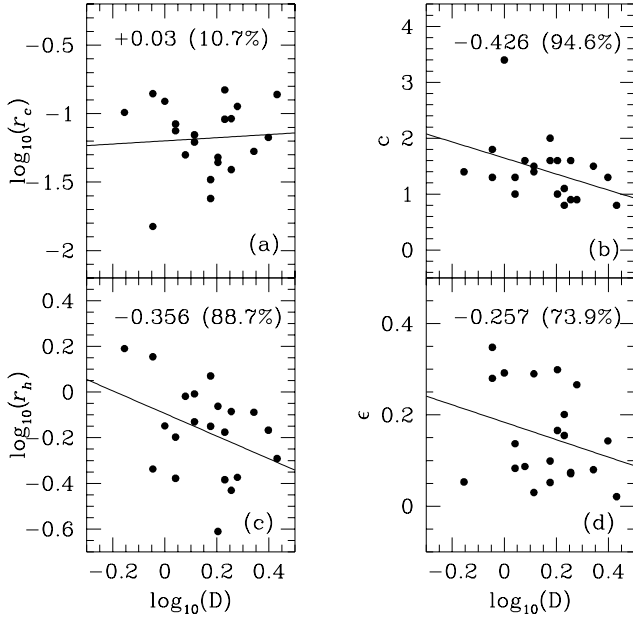


Fig. 15. This figure shows the relationships between four properties of the NGC 5128 GC candidates and their observed distance, D , from the center of NGC 5128. The Spearman rank correlation coefficients, and the confidence levels for rejecting the hypothesis that the observed correlations are due to chance, are shown at the top of each panel. The lines show the best-fitting straight lines to the data. Panel (a) shows the core radius (in arcseconds), panel (b) shows the central concentration, panel (c) shows the half-mass radius (in arcseconds) of the best-fitting single-mass Michie–King model, and panel (d) shows the ellipticity.

4. Colors

4.1. The Photometry

Performing accurate photometry on the NGC 5128 GC candidates is difficult. These GC candidates are extended objects, not point sources, so it is not possible to determine their magnitudes simply by fitting a scaled PSF to each candidate. Since each GC candidate has a unique size *and* radial profile (parameterized by the concentration, c), aperture photometry with a single aperture will not return accurate magnitudes. Therefore, we elected to use the total flux in the best-fitting Michie–King model as the best estimate of its flux.

We converted the total instrumental fluxes to the standard Johnson–Cousins VI magnitudes using the prescription of Holtzman et al. (1995). The calibration equations we used are:

$$V = -2.5 \log_{10}(C_{F555W}) + (-0.052 \pm 0.007)(V - I)_0 \\ + (0.027 \pm 0.002)(V - I)_0^2$$

$$+ (21.725 \pm 0.005) + 2.5 \log_{10}(G_i), \quad (8)$$

$$I = -2.5 \log_{10}(C_{F814W}) + (-0.062 \pm 0.009)(V - I)_0 \\ + (0.025 \pm 0.002)(V - I)_0^2 \\ + (20.839 \pm 0.006) + 2.5 \log_{10}(G_i), \quad (9)$$

where C is the count rate in ADU/second after correcting for charge transfer efficiency (CTE) effects. We applied the CTE corrections of Whitmore & Heyer (1997) for a five pixel aperture. G is the gain ratio between the $14 e^-$ gain state (which was used for the calibration observations) and the $7 e^-$ gain state (which was used for the NGC 5128 observations). As discussed in Holtzman et al. (1995), reddening corrections need to be applied *before* the instrumental magnitudes are calibrated to the standard Johnson–Cousins system. This is because the WFPC2 filters have different band passes and effective wavelengths than those of the standard V and I filters. We adopted a foreground reddening in the direction of NGC 5128 of $E_{B-V} = 0.11 \pm 0.02$ from the reddening maps of Burstein & Heiles (1982) and assumed $E_{V-I} = 1.36 E_{B-V}$ (Taylor 1986; Fahlman et al. 1989). We used the extinction corrections for K0III stars from Table 12 of Holtzman et al. (1995) to obtain $A_V = 0.340$ and $A_I = 0.201$.

Fig. 16 shows the distribution of colors for our 21 GC candidates, and for 62 spectroscopically confirmed GCs in NGC 5128 (HG92). We converted the HG92 $C - T_1$ colors to $V - I$ colors using $V - I = 0.115 + 0.514(C - T_1)$ (Geisler 1996). The VI magnitudes determined this way should be treated with caution since Geisler (1996) found that $C - T_1$ colors do not reproduce $V - I$ colors particularly well. There is only one object (#12, $V = 20.30 \pm 0.03$, $V - I = 0.40 \pm 0.04$) which appears significantly bluer than the other GC candidates. Based on its color this object may be a young GC. Visual inspection of the WFPC2 images (see Fig. 5) shows that this object appears to be a normal GC in NGC 5128. The V - and I -band photometry of all of our GC candidates are listed in Table 8. The R -, J -, H -, and K -band photometry from AM97 are also given.

4.2. Reddening Within NGC 5128

In order to estimate the amount of internal reddening within NGC 5128 in the direction of each GC candidate we determined the color of the background near each object. This was done by letting the mean background color be a free parameter during the Michie–King model fitting process. The expected unreddened $V - I$ color at the location of each GC candidate was then subtracted from the observed mean background color to get an estimate of the internal reddening. The expected color of the background that each GC candidate sits on was determined as follows.

Table 8. Photometry for the GC candidates in NGC 5128.

ID	V	I	$V-I$	R	J	H	K
1	19.33 ± 0.02	18.42 ± 0.02	0.91 ± 0.03
2	18.21 ± 0.02	17.22 ± 0.02	0.99 ± 0.02
3	21.32 ± 0.04	19.94 ± 0.03	1.38 ± 0.05
4	21.42 ± 0.04	19.31 ± 0.03	2.11 ± 0.05
5	19.76 ± 0.02	18.49 ± 0.02	1.27 ± 0.03
6	19.40 ± 0.02	17.58 ± 0.02	1.82 ± 0.03
7	20.91 ± 0.03	19.51 ± 0.03	1.40 ± 0.04
8	20.08 ± 0.03	19.11 ± 0.02	0.97 ± 0.04
9	19.25 ± 0.02	18.21 ± 0.02	1.04 ± 0.03	19.17	17.98 ± 0.28	17.62 ± 0.45	...
10	19.54 ± 0.02	18.39 ± 0.02	1.15 ± 0.03	19.62	17.70 ± 0.19	16.68 ± 0.15	16.56 ± 0.26
11	19.45 ± 0.02	18.05 ± 0.02	1.40 ± 0.03
12	20.30 ± 0.03	19.90 ± 0.03	0.40 ± 0.04	20.51	18.56 ± 0.38	17.74 ± 0.38	...
13	18.77 ± 0.02	17.62 ± 0.02	1.15 ± 0.03
14	20.01 ± 0.02	19.15 ± 0.02	0.86 ± 0.03	20.05	16.87 ± 0.16	16.62 ± 0.30	16.19 ± 0.25
15	17.56 ± 0.02	16.44 ± 0.02	1.12 ± 0.03	17.39	15.87 ± 0.07	15.13 ± 0.06	14.96 ± 0.08
16	18.45 ± 0.02	17.52 ± 0.02	0.93 ± 0.03	18.53	17.00 ± 0.12	16.27 ± 0.12	16.66 ± 0.24
17	20.72 ± 0.03	19.64 ± 0.03	1.08 ± 0.04
18	17.07 ± 0.02	16.08 ± 0.02	0.99 ± 0.03	17.09	15.49 ± 0.05	14.93 ± 0.04	14.58 ± 0.05
19	19.97 ± 0.03	17.78 ± 0.03	2.19 ± 0.04
20	20.03 ± 0.03	17.65 ± 0.03	2.38 ± 0.04
21	18.41 ± 0.02	17.41 ± 0.02	1.00 ± 0.03

From Fig. 5 of van den Bergh (1976) we derived

$$B - V = 0.153 \log_{10}(D) + 0.924, \quad (10)$$

where D is the projected distance from the center of NGC 5128 in arcminutes. We estimate that the uncertainty in the $B - V$ values from Eq. 10 is $\sim \pm 0.1$. The $B - V$ colors were converted to $(V - I)_0$ colors by subtracting the adopted Milky Way reddening of $E_{B-V} = 0.11 \pm 0.02$ and using

$$(V - I)_0 = 0.745(B - V)_0 + 0.399, \quad (11)$$

which we derived from the Galactic Globular Cluster Catalogue of W. Harris (1996). For each GC candidate in NGC 5128 we computed the expected background color using Eqs. 10 and 11 and subtracted this from the mean color of the unresolved background around each GC candidate. The internal reddening due to dust in NGC 5128 was then computed by subtracting the expected color from the observed color for each GC candidate. The internal reddenings, as well as the dereddened V_0 and $(V - I)_0$ values for each GC candidate, are listed in Table 9. The V_0 and $(V - I)_0$ values are corrected for both the Burstein & Heiles (1982) reddening *and* our estimate of the internal reddening in NGC 5128. The uncertainty in each reddening estimate is ~ 0.08 and negative internal reddenings were set to $E_{V-I} = 0$.

In order to check these differential reddenings, we repeated our calculation using the color of a typical galaxy with the same morphological type as NGC 5128. The

Table 9. The estimated internal reddening within NGC 5128 along the line of sight, the dereddened V -band magnitude, and the dereddened $(V - I)_0$ color for each GC candidate.

ID	E_{V-I}	$V_0 \pm \sigma_{V_0}$	$(V - I)_0 \pm \sigma_{(V-I)_0}$
1	0.17	18.94 ± 0.06	0.74 ± 0.08
2	0.15	17.87 ± 0.06	0.84 ± 0.08
3	0.06	21.18 ± 0.07	1.31 ± 0.09
4	0.00	21.42 ± 0.07	2.12 ± 0.10
5	0.00	19.76 ± 0.06	1.27 ± 0.09
6	0.07	19.25 ± 0.06	1.75 ± 0.09
7	0.14	20.59 ± 0.07	1.27 ± 0.09
8	0.06	19.94 ± 0.06	0.90 ± 0.09
9	0.08	19.08 ± 0.06	0.96 ± 0.08
10	0.11	19.28 ± 0.06	1.03 ± 0.09
11	0.09	19.26 ± 0.06	1.32 ± 0.09
12	0.14	19.98 ± 0.06	0.26 ± 0.09
13	0.10	18.53 ± 0.06	1.04 ± 0.08
14	0.10	19.77 ± 0.06	0.76 ± 0.09
15	0.06	17.42 ± 0.06	1.06 ± 0.08
16	0.14	18.13 ± 0.06	0.79 ± 0.08
17	0.13	20.42 ± 0.07	0.95 ± 0.09
18	0.10	16.83 ± 0.06	0.89 ± 0.08
19	0.10	19.76 ± 0.07	2.10 ± 0.09
20	0.00	20.03 ± 0.07	2.38 ± 0.09
21	0.22	17.91 ± 0.06	0.78 ± 0.08

Third Reference Catalogue of Bright Galaxies (de Vaucouleurs et al 1991) lists NGC 5128 as being an intermedi-

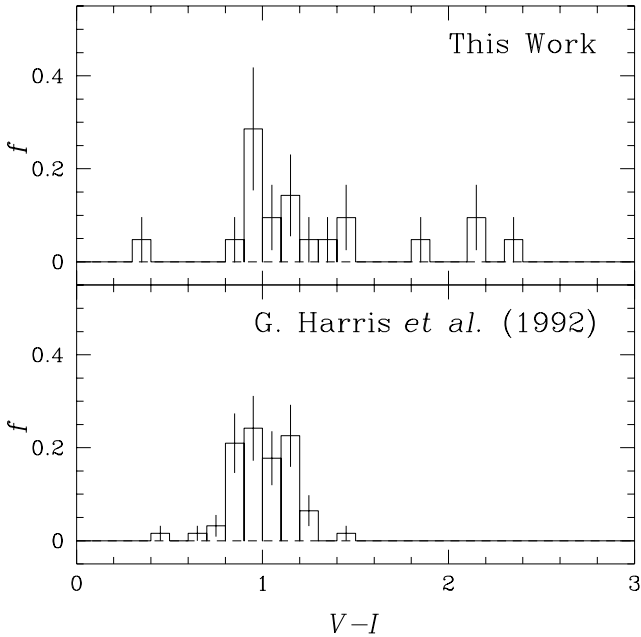


Fig. 16. The upper panel shows the distribution of colors for our 21 GC candidates in NGC 5128 while the lower panel shows the distribution of colors for 62 spectroscopically confirmed GCs in NGC 5128 from HG92. The colors have been corrected for reddening in the Milky Way in the direction of NGC 5128, but not for internal reddening in NGC 5128 itself.

ate S0 galaxy with a morphological type of $T = -2 \pm 0.3$. Buta & Williams (1995) find a mean color for $T = -2$ galaxies of $\langle V-I \rangle_{\text{total}} = 1.145 \pm 0.069$ based on a sample of 55 galaxies. This is within 1σ of the expected background colors derived from the observed color gradient in the outer regions of NGC 5128. If we assume that the unresolved light from NGC 5128 is the same as that from a typical $T = -2$ galaxy, but has been reddened due to the presence of dust from the merger, then the excess reddening can be estimated by subtracting the mean color of a $T = -2$ galaxy from the observed color of the unresolved background around each GC candidate. The differential reddening that we obtain by assuming that NGC 5128 is a $T = -2$ galaxy are consistent with those obtained using the van den Bergh (1976) color gradient.

The first problem with this method of estimating the internal reddening in NGC 5128 is that NGC 5128 is not a normal elliptical galaxy, but an elliptical galaxy that has undergone a merger with a small late-type spiral galaxy. Therefore, the unresolved light near the center will be a combination of light from the original galaxy and from stars in the captured spiral galaxy. In our derivations of the internal reddening we have assumed that the only changes in the color of the central regions of NGC 5128 are those due to dust, and ignored changes in color due to star formation and differences in the underlying stellar

population. Buta & Williams (1995) list mean colors for late spiral galaxies of $\langle V-I \rangle_{\text{total}} \sim 0.8$ to 0.7 , depending on the morphological type of the spiral. Therefore, the contribution from the merged spiral galaxy will cause the actual unreddened color of the unresolved background in NGC 5128 to be as much as a few tenths of a magnitude bluer than we have assumed. This will lead us to underestimate the internal reddening within NGC 5128 by a few tenths of a magnitude. It is possible that some of the GC candidates are being seen against regions of recent star formation in NGC 5128. This would also lead us to underestimate the internal reddening by a few tenths of a magnitude.

A second problem is that the structure of the dust features in NGC 5128 changes on spatial scales of less than $\sim 1''$. The mean tidal radius of the GC candidates is $\bar{r}_t = 1''.42 \pm 0''.15$ (se), and the surface brightness of the background was determined while fitting the Michie-King models by taking the mean value of the pixels that fell within the fitting box (64×64 pixels) but beyond the tidal radius. Therefore, small-scale spatial structure in the dust lane could introduce errors of several tenths of a magnitude in our estimates of the internal reddening in NGC 5128.

Finally, the reddening corrections are not being made in the WFPC2 photometric system. This may introduce small errors in the reddening corrections that we determine. We believe, however, that these errors will be small compared to other uncertainties in the method. In light of these uncertainties we believe that it is possible that our estimates of the differential reddening for each GC candidate are only accurate to $\sim \pm 0.3$ mag.

Fig. 17 shows the color distribution of the GC candidates after correcting for internal reddening within NGC 5128. There appear to be three populations in the upper panel of Fig. 17. The largest population is centered at $(V-I)_0 \sim 1.0$ and contains 16 of the 21 GC candidates. This population appears to be similar to the spectroscopically confirmed GCs of HG92 and probably represents a genuine old population of GCs in NGC 5128. The similarity between the colors of these GC candidates and the dereddened colors of the Milky Way GCs suggests that this population is not heavily reddened and therefore probably lies on the near side of NGC 5128. The second component is the four objects with $(V-I)_0 > 1.4$. These objects are probably GCs that are being seen through large amounts of dust in NGC 5128. Alternately, they could be background galaxies that have been misidentified as GC candidates. The third component is the single blue object with $(V-I)_0 = 0.26 \pm 0.09$. An examination of the image of this object (Fig. 5) suggests that it is a legitimate GC candidate so its blue color makes it the best candidate for being a young GC in our sample.

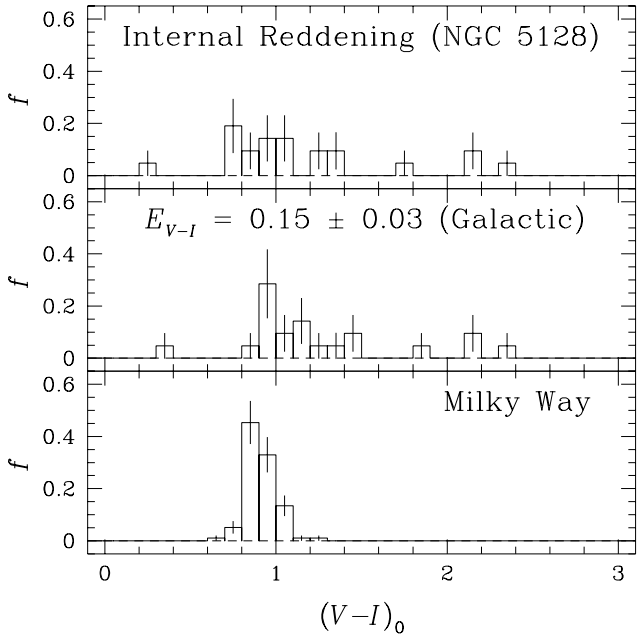


Fig. 17. The upper panel shows the distribution of colors for the GC candidates in NGC 5128 after correcting for the estimated internal reddening due to dust in NGC 5128. The middle panel shows the distribution of colors for the GC candidates without any correction for internal reddening within NGC 5128 (but with a correction for Galactic reddening in the direction of NGC 5128). The lower panel shows the distribution of dereddened colors for the Milky Way GC system.

4.3. Iron Abundance

The iron abundance for each GC candidate was estimated using

$$[\text{Fe}/\text{H}] = -6.568 + 6.733(V-I)_0 - 1.372(V-I)_0^2, \quad (12)$$

which was determined from 45 Galactic GCs with low reddenings and good metallicity estimates, and from 13 metal-rich GCs in NGC 1399 (Kissler-Patig et al. 1998).

If the blue color of object #12 is due solely to its iron abundance, then it has $[\text{Fe}/\text{H}] = -4.91 \pm 0.54$. This implausibly low iron abundance suggests that age is primarily responsible for at least some of the blue color, supporting the notion that #12 is a young object. The mean iron abundance of the 16 GC candidates with $0.6 \leq (V-I)_0 \leq 1.4$ is $[\text{Fe}/\text{H}] = -1.27 \pm 0.20$ (se), which is within 2σ of the $[\text{Fe}/\text{H}] = -0.8 \pm 0.2$ value found by HG92. This suggests that the colors of these objects are consistent with them being old GCs, or moderately reddened intermediate-age GCs. The four objects with $(V-I)_0 > 1.4$ all have iron abundances of greater than the Solar value ($[\text{Fe}/\text{H}] = +1.44 \pm 0.15$). This suggests that the red colors of these objects are primarily due to dust along the line of sight within NGC 5128, not high

iron abundances, although we can not rule out the possibility that at least some of these GC candidates have high iron abundances.

5. Young GCs in NGC 5128

We would expect young GCs to be brighter and bluer than their old counterparts, although reddening uncertainties complicate the interpretation of the observed colors for the NGC 5128 GC candidates. The mean $(V-I)_0$ color of the 97 Milky Way GCs that have both $V-I$ and E_{B-V} values listed in the catalogue of W. Harris (1996) is 0.91 ± 0.09 (standard deviation). This is consistent with the colors of the majority of the GC candidates that we found in the inner regions of NGC 5128.

Schweizer & Seitzer (1993) find that young GCs in NGC 7252 have $V-I$ colors that are ~ 0.5 mag bluer than old GCs, which suggests that objects in NGC 5128 with colors bluer than $V-I \sim 0.8$ may be young ($t_0 < 1$ Gyr) GCs. We find five objects with $(V-I)_0 < 0.8$. One of these, object #12, is unusually blue, with $(V-I)_0 = 0.26 \pm 0.09$. AM97 identified this object as M23 and measured a $J-H$ color of 0.83. A visual examination of the *HST* images (see Fig. 5) shows nothing unusual about this object. If we assume that the blue color of this object is due to it being a young star cluster, we can use the models of Bruzual & Charlot (1993) to estimate its age and mass from its $(V-I)_0$ color and its integrated V magnitude. Fig. 18a shows the evolution of the $(V-I)_0$ color of star clusters for several iron abundances. This figure suggests an age for #12 of less than ~ 100 Myr, while Fig. 18b suggests that, if it is a young, metal-poor GC, it will fade by between ~ 4 and ~ 6.5 mag over the next 12 Gyr. Therefore, when object #12 is as old as a typical Milky Way GC (~ 12 Gyr), it will have M_V between ~ -3.5 and -1 , corresponding to a mass of between ~ 4000 and ~ 400 Solar masses, assuming a mass-to-light ratio of two. W. Harris (1996) lists four Galactic GCs with masses less than 4000 Solar masses: AM 1 with a mass of 700 Solar masses, Pal 1 with a mass of 1000 Solar masses, E 3 with a mass of 2100 Solar masses, and Terzan 1 with a mass of 3400 Solar masses, although these mass determinations are highly uncertain. In light of the small mass for object #12 it is also possible that this object is a massive open cluster.

The sixteen GC candidates with $0.7 \leq (V-I)_0 < 1.4$ have colors that are consistent with being young (< 1 Gyr), intermediate-aged (1–4 Gyr), or old (> 4 Gyr) GCs depending on the iron abundances and reddenings that are assumed. If these GC candidates have iron abundances similar to those found in the Galactic GCs ($[\text{Fe}/\text{H}] < 0$) then Fig. 18a suggests that their observed $(V-I)_0$ colors are consistent with them having ages of > 1 Gyr. If this is the case then Fig. 18b suggests that these objects will fade by between ~ 0 and 2 mag in V by the time they are ~ 12 Gyr old. This corresponds to these GC candidates having

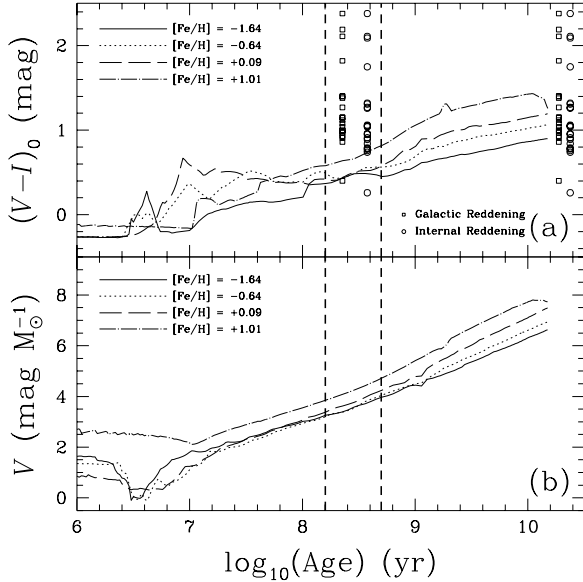


Fig. 18. The upper panel shows the time evolution of $(V-I)_0$ for GCs with a Salpeter Initial Mass Function for a range of cluster masses from 0.1 to 125 Solar masses, and a range of iron abundances from $[\text{Fe}/\text{H}] = -1.64$ to $[\text{Fe}/\text{H}] = +1.01$, using the models of Bruzual & Charlot (1993). The heavy vertical lines are at 160 Myr and 500 Myr respectively (the interval that the most recent merger most likely occurred in). The colors of the 21 GC candidates are plotted as squares (Galactic reddening removed) and circles (Galactic and internal reddening within NGC 5128 removed). The lower panel shows the time evolution of the V magnitude per Solar mass using the same models.

masses between $\sim 40\,000$ and $\sim 4\,000\,000$ Solar masses, which is consistent with the masses of Galactic GCs. If, on the other hand, the objects have iron abundances greater than the Solar value then their colors are consistent with their being young GCs. In this case Fig. 18b suggests that they will fade by ~ 3 to 4 mag in V over then next 12 Gyr, which would give them masses of between $\sim 5\,000$ and $\sim 250\,000$ Solar masses.

These results assume that the differential reddenings derived in Sect. 4.2 are uncertain by $\sim \pm 0.3$ mag, and may contain systematic uncertainties of a few tenths of a magnitude. The $(V-I)_0$ colors of the sixteen GC candidates with $0.7 \leq (V-I)_0 < 1.4$ are most consistent with young GCs if the differential reddenings have been systematically underestimated by between 0.1 and 0.7 mag. If our estimates of the differential reddening for these objects are correct then their $(V-I)_0$ colors suggest that these GC candidates are normal, old, metal-poor GCs. Spectroscopic observations are needed to break the degeneracy between reddening and metallicity to accurately determine the ages of these objects.

The red colors, and high implied iron abundances, of the four GC candidates with $(V-I)_0 \geq 1.4$ suggest that these objects are heavily reddened. If we assume that all of these objects are young, metal rich clusters that formed at the time of the merger event then differential reddenings of $E_{V-I} \sim 1.1$ to 1.8, in addition to those derived in Sect. 4.2, are required to account for their observed red colors. This corresponds to between ~ 2.4 and ~ 3.9 mag of extra extinction in the V band. If, on the other hand, these objects are young metal poor clusters then the amount of additional differential reddening required to account for their observed red colors is between ~ 1.3 and ~ 2.1 mag. It is unlikely that we have underestimated the differential reddening by this amount. If we assume that these objects are old GCs (~ 12 Gyr) seen through dust then we have underestimated the amount of differential reddening by between ~ 0.4 and ~ 1.4 mag. It is possible that a combination of random and systematic uncertainties in the differential reddening calculations could result in us underestimating the reddenings of these objects by several tenths of a magnitude, so we can not rule out the possibility that these four objects are old GCs. Another possibility is that they are background red elliptical, or dwarf elliptical galaxies with concentrations similar to those of the Galactic GCs. Spectroscopic observations are needed to confirm the nature of these objects.

In summary, the dereddened $(V-I)_0$ color of object #12 is consistent with it being either a small young GC or a massive open cluster. The sixteen objects with $0.8 \leq (V-I)_0 < 1.4$ have colors that are consistent with them being either young GCs which suffer from up to ~ 0.7 mag of differential reddening or old GCs that suffer from up to ~ 0.2 mag of differential reddening. Spectroscopic observations will be needed to determine the ages of these GC candidates. The four objects with $(V-I)_0 > 1.4$ are either old heavily reddened GCs or background galaxies that have similar concentrations to Galactic GCs.

6. Conclusions

We have used the *HST*/WFPC2 to identify 21 GC candidates in a $25''$ area centered on the nucleus of the nearest giant elliptical galaxy, NGC 5128. There is strong evidence that this galaxy has undergone a merger with a small late-type spiral between ~ 160 and 360 Myr ago. We fit two-dimensional, PSF-convolved, single-mass Michie-King models to each GC candidate and derived core radii, tidal radii, half-mass radii, ellipticities, and position angles for each object. We assumed that the GC candidates were structurally similar to those in the Local Group; i.e., they could be well fit by Michie-King models, and had similar half-mass radii and ellipticities. Therefore, only objects with structural parameters similar to those of GCs in the Local Group were accepted as being GC candidates. It is possible that we have missed NGC 5128 GC candidates that are significantly less centrally concentrated than the

GCs in the Local Group. However, since we were primarily interested in using the colors of the GC candidates to estimate their ages we preferred to risk rejecting legitimate GC candidates rather than risk having our sample contaminated with stars and background galaxies. Within this constraint we find no evidence that the NGC 5128 GC candidates have core-, half-mass-, or tidal radii that are distributed differently from those GCs in the Milky Way that do not exhibit central brightness cusps. There is weak evidence that NGC 5128 GC candidates are systematically more elliptical than are the Galactic GCs.

We have obtained V - and I -band photometry for all 21 of our GC candidates. We find no evidence for the bimodal color distribution observed among GCs at larger distances from the center of NGC 5128 (HG92; Zepf & Ashman 1993), although this is likely due to the small sample size (21 objects), the poor metallicity sensitivity of the $V-I$ color index, and confusion due to differential reddening within NGC 5128.

We have identified one very blue GC candidate (#12) with $(V-I)_0 = 0.26 \pm 0.09$. Using a color-age relation derived from the models of Bruzual & Charlot (1993), we estimate that this object has an age of less than ~ 100 Myr and a mass of between ~ 400 and ~ 4000 Solar masses, which is barely consistent with this object being a small GC that formed during the merger event. There are sixteen objects with $0.7 \leq (V-I)_0 < 1.4$ that have colors and integrated magnitudes that are consistent with their being either young GCs that formed during the merger event or old GCs similar to those found in the Milky Way, depending on what we assume about their iron abundances and differential reddenings. The colors of these GCs are very similar to those measured by HG92, but the amount of reddening for each object is uncertain by ~ 0.3 mag. There are four GC candidates with $(V-I)_0 > 1.4$, which imply either implausibly high metallicities or very large differential reddenings. We can not rule out the possibility that some of these four objects are background galaxies seen through the central regions of NGC 5128.

Spectroscopic studies will be needed to determine unambiguously if any of the central GC candidates in NGC 5128 are young GCs that may have formed as a result of the merger. If young GCs in NGC 5128 can be unambiguously identified spectroscopically, and their ages determined, this will make it possible to estimate the amount of time required for GCs to form after a galactic merger has occurred.

Acknowledgements. This research is based on observations made with the NASA/ESA *Hubble Space Telescope* obtained at the Space Telescope Science Institute. STScI is operated by the Association of Universities for Research in Astronomy Inc. under NASA contract NAS 5-26555. S. H. is supported by the Danish Centre for Astrophysics with the *HST*. P. C. acknowledges financial support from the Sherman M. Fairchild Foundation. The authors would like to thank Peter Stetson for

kindly making his WFPC2 PSFs, and the DAOPHOT II software, available.

References

- Alonso M. V., Minniti D. 1997, ApJS 109, 397 (AM97)
 Bahcall J. N., Soneira R. M. 1981, ApJS 47, 357
 Bruzual A. G., Charlot S. 1993, ApJ 405, 538
 Burstein D., Heiles, C. 1982, AJ 87, 1165
 Buta R., & Williams K. 1995, AJ 109, 543
 Chaboyer B., Demarque P., Kernan P. J., Krauss L. M. 1998, ApJ 494, 96 (astro-ph/9706128)
 Cohn, H. 1979, ApJ 234, 1036
 de Vaucouleurs G., de Vaucouleurs A., Corwin H. G., Jr., et al. 1991, Third Reference Catalogue of Bright Galaxies, Springer, New York
 Djorgovski S., Meylan G. 1994, AJ 108, 1292
 Ebner K., Balick B. 1983, PASP 95, 675
 Fahlman G. G., Richer H. B., Searle L., Thompson I. B. 1989, ApJL 343, L49
 Geisler D. 1996, AJ 111, 480
 Geisler D., Hodge P. 1980, ApJ 242, 66
 Graham J. A., Philips M. M. 1980, ApJL 239, L97
 Grillmair C. J., Freeman K. C., Irwin M., Quinn P. J. 1995, AJ 109, 2553 (astro-ph/9502039)
 Grillmair C. J., Ajhar E. A., Faber S. M., et al. 1996, AJ 111, 2293 (astro-ph/9602047)
 Harris W. E. 1996, AJ 112, 1487
 Harris H. C., Harris G. L. H., Hesser J. E., MacGillivray H. T. 1984, ApJ 287, 185
 Harris H. C., Harris G. L. H., Hesser J. E. 1988, in: Globular Cluster Systems in Galaxies, AU Symp. 126, eds: J. E. Grindley and A. G. D. Philip, Kluwer, Dordrecht, p. 205
 Harris G. L. H., Geisler D., Harris H. C., Hesser J. E. 1992, AJ 104, 613 (HG92)
 Harris G. L. H., Poole G. B., Harris W. E. 1998, AJ 116, 2866 (astro-ph/9806390)
 Harris G. L. H., Harris W. E., Poole G. B. 1999, AJ 117, 855 (astro-ph/9810134)
 Heggie D. C., Ramamani N. 1995, MNRAS 272, 317
 Holland S. 1997, Ph.D. Thesis, University of British Columbia
 Holland S., Fahlman G. G., Richer H. B. 1997, AJ 114, 1488 (astro-ph/9708232)
 Holtzman J. A., Faber S. M., Shaya E. J., et al. 1992, AJ 103, 691
 Holtzman J. A., Burrows C. J., Casertano S., et al. 1995, PASP 107, 1065
 Hui X., Ford H. C., Freeman K. C., Dopita M. A. 1995, ApJ 449, 592
 Innanen K. A., Harris W. E., Webbink R. F. 1983, AJ 88, 338
 Israel F. P. 1998, A&AR 8, 237 (astro-ph/9811051)
 Johnston K. J. et al. 1995, AJ 110, 880
 King I. R. 1966, AJ 71, 64
 Kissler-Patig M., Brodie J. P., Schroder L. L., et al. 1998, AJ 115, 105 (astro-ph/9710117)
 Lutz D. 1991, A&A 245, 31
 Michie R. W. 1963, MNRAS 125, 127
 Minniti D., Alonso M. V., Goudfrooij P., Jablonka P., Meylan, G. 1996, ApJ 467, 221 (astro-ph/9604017)
 Moffat A. F. J. 1969, A&A 3, 455
 Murray S. D., Lin D. N. C. 1992, ApJ 400, 265

- Odenkirchen M., Brosche P., Geffert M., Tucholke H.-J. 1997, *New Astronomy* 2, 477
- Quillen A. C., Graham J. R., Frogel J. A. 1993, *ApJ* 412, 550
- Schreier E. J., Capetti A., Macchetto F., Sparks W. B., Ford H. J. 1996, *ApJ* 459, 535
- Schweizer F., Seitzer P. 1993, *ApJL* 417, L29
- Schweizer F., Miller B. W., Whitmore B. C., Fall S. M. 1996, *AJ* 112, 1839
- Secker J. 1995, *PASP* 107, 496
- Sharples R. 1988, in: *Globular Cluster Systems in Galaxies*, IAU Symp. 126, eds: J. E. Grindley and A. G. D. Philip, Kluwer, Dordrecht, p. 545
- Soria R. et al. 1996, *ApJ* 465, 79
- Stetson P. B. 1987, *PASP* 99, 191
- Stetson P. B. 1994, *PASP* 106, 250
- Suchkov A., Casertano S. 1997, *WFPC2 Instrument Science Report WFPC2 97-01*
- Takahashi K. 1997, *PASJ* 49, 547
- Taylor B. J. 1986, *ApJS* 60, 577
- Tubbs A. D. 1980, *ApJ* 241, 969
- Tyson J. A. 1988, *AJ* 96, 1
- van den Bergh S. 1976, *ApJ* 208, 673
- van den Bergh S., Morbey C., Pazder J. 1991, *ApJ* 375, 594
- White R. E., Shawl S. J. 1987, *ApJ* 317, 246
- Whitmore B. C., Heyer I. 1997, *STScI ISR WFPC2 97-08*
- Zepf S. E., & Ashman K. M. 1993, *MNRAS* 264, 611

This figure "h1383f5.jpg" is available in "jpg" format from:

<http://arxiv.org/ps/astro-ph/9906247v1>

This figure "h1383f6.jpg" is available in "jpg" format from:

<http://arxiv.org/ps/astro-ph/9906247v1>

This figure "h1383f7.jpg" is available in "jpg" format from:

<http://arxiv.org/ps/astro-ph/9906247v1>

This figure "h1383f8.jpg" is available in "jpg" format from:

<http://arxiv.org/ps/astro-ph/9906247v1>

This figure "h1383f9.jpg" is available in "jpg" format from:

<http://arxiv.org/ps/astro-ph/9906247v1>

This figure "h1383f10.jpg" is available in "jpg" format from:

<http://arxiv.org/ps/astro-ph/9906247v1>